This article has been accepted for publication in a future issue of this journal, but has not been fully edited. Content may change prior to final publication. Citation information: DOI 10.1109/JSEN.2019.2947489, IEEE Sensors Journal

Fuzzy Adaptive Attitude Estimation for a Fixed-Wing UAV with a Virtual SSA Sensor During a GPS Outage

Wonkeun Youn, Matthew B. Rhudy, Am Cho, and Hyun Myung, *Senior Member, IEEE*

***Abstract*—This paper proposes a novel robust attitude estimation algorithm for a small unmanned aerial vehicle (UAV) in the absence of GPS measurements. A synthetic sideslip angle (SSA) measurement formulated for use under the zero-angle assumption is newly proposed for a UAV without angle-of-attack (AOA)/SSA sensors to enhance the state estimation performance during a GPS outage. In addition, the nongravitational acceleration is estimated using the proposed Kalman filter and is then subtracted from the raw acceleration to yield a reliable gravity estimate. Then, a fuzzy-logic-aided adaptive measurement covariance matching algorithm is devised to adaptively reduce the weight given to disturbed acceleration and magnetic field measurements in the attitude estimation, yielding the fuzzy adaptive error-state Kalman filter (FAESKF) algorithm. Experimental flight results demonstrate that the proposed FAESKF algorithm achieves a remarkable improvement in attitude estimation compared to the conventional algorithm.**

***Index Terms*—Attitude estimation, Error-state Kalman filter (ESKF), Fuzzy, GPS outage, Inertial measurement unit (IMU), Navigation, Unmanned aerial vehicle (UAV).**

I. Introduction

RELIABLE and accurate attitude estimation in the attitude and heading reference system (AHRS) is indispensable for the autonomous navigation and control of small unmanned aerial vehicles (UAVs) [1]. Microelectromechanical system (MEMS)-based inertial measurement units (IMUs), which include three-axis accelerometers, three-axis gyroscopes, and three-axis magnetometers, have received considerable attention as attractive solutions for small UAVs due to their light weight, small scale, low power consumption, and low cost [2], [3]. An IMU-based inertial navigation system (INS) can yield a stable state estimation within a short time period [4], but the error of the INS will accumulate over time due to the various drawbacks of MEMS-based IMUs, such as their time-varying biases, scaling factors, cross-coupling errors, and random noise, which result in significant drift [5]. To address these issues, GPS receivers that provide absolute position/velocity updates have been commonly utilized to correct for INS drift [6].

The algorithms that are most commonly employed to obtain reliable and accurate attitude estimates can be divided into two categories: constant gain observers, known as complementary filters, and extended Kalman filters (EKFs). A complementary filter is a multisensor fusion algorithm that integrates the angular rate from a gyroscope and then corrects the gyroscope bias [7]. The roll and pitch angles can be extracted by fusing accelerometer measurements, and the yaw angle can be derived from magnetometer measurements [8]. The states of a complementary filter are commonly defined as attitude-representative states, such as Euler angles or quaternions and gyro biases [9]. A complementary filter requires relatively simple algorithms, requires little computation power, and is easy to implement. These features make this approach suitable for low-cost embedded systems [10].

Another approach to attitude estimation is an EKF algorithm based on a federated architecture (combining attitude and position/velocity estimation), which is designed to take advantage of all sensor measurements [11]. Such an EKF-based algorithm has the potential to achieve improved attitude estimation performance if it is tuned properly. Although complementary filters have several advantages over EKF-based algorithms, such as their simplicity and ease of tuning and implementation, an EKF-based algorithm is the preferred approach since it is capable of fusing data from a wide variety of sensor types and detecting statistically significant inconsistencies in the measurements for the diagnosis of sensor faults in the Kalman filter framework [12].

The abovementioned algorithms produce reasonably stable attitude estimation results when GPS measurements are available, but their estimation performance cannot be guaranteed during a GPS outage since the absolute position/velocity measurements provided by a GPS receiver play a key role in the attitude estimation procedure. To address this issue, a complementary filter for attitude estimation for a fixed-wing UAV without GPS capabilities has been presented [7]. In that study, the centripetal acceleration was computed using

This research was supported by Unmanned Vehicles Advanced Core Technology Research and Development Program through the National Research Foundation of Korea (NRF), Unmanned Vehicle Advanced Research Center (UVARC) funded by the Ministry of Science and ICT, the Republic of Korea (NRF-2017M1B3A2A01049995) and in part by First-Mover Program for Accelerating Disruptive Technology Development (NRF-2018M3C1B9088328). This work was also partially supported by BK21+.

Wonkeun Youn and Am cho are with the UAV System Division, Aeronautics Research and Development Head Office, Korea Aerospace Research Institute, Yuseong-gu, Daejeon, 34133, Republic of Korea (e-mail: wkyoun@kari.re.kr, cho1838@kari.re.kr). Matthew Rhudy is with the Division of Engineering, Business, and Computing at the Pennsylvania State University, Reading, PA 19610, USA (e-mail: matthew.rhudy@gmail.com). Hyun Myung and Wonkeun Youn are with the Urban Robotics Laboratory (URL), Korea Advanced Institute of Science and Technology (KAIST), 291 Daehak-ro, Yuseong-gu, Daejeon, 34141, Republic of Korea (e-mail: hmyung@kaist.ac.kr; won13y@kaist.ac.kr) (corresponding author to provide phone: +82-42-350-3630; fax: +82-42-350-3610; e-mail: hmyung@kaist.ac.kr).

1558-1748 (c) 2019 IEEE. Personal use is permitted, but republication/redistribution requires IEEE permission. See http://www.ieee.org/publications_standards/publications/rights/index.html for more information.

This article has been accepted for publication in a future issue of this journal, but has not been fully edited. Content may change prior to final publication. Citation information: DOI 10.1109/JSEN.2019.2947489, IEEE Sensors Journal

airspeed measurements and a simple first-order model of the angle of attack (AOA) and was then subtracted from the raw acceleration, yielding better attitude estimation results. However, this approach did not consider the wind states in the state definition of the complementary filter, thus limiting the performance improvement that could be achieved. In another study, a centripetal force model was developed to estimate the motion acceleration in order to correct the accelerometer measurements during a GPS outage [13]. Specifically, the compensated gravity vector, magnetic heading, barometric height, and ground velocity were fused in the EKF framework, and the validity of this approach was verified by hardware-in-the-loop simulations. The translational acceleration was ignored in that study; however, the motion acceleration needs to be estimated to obtain a high-accuracy gravity vector for an accelerating/decelerating UAV [14].

As alternatives to the approaches discussed above, a neural-network-based algorithm and a Gaussian process regression approach have recently been proposed to address the problem of GPS outages [15], [16]. In addition, the auto-regressive integrated moving average (ARIMA) model and an offline-trained extreme learning machine (ELM) model combined with the interacting multiple model (IMM) have been investigated for predicting the INS errors during a GPS outage while switching among three bias filters to account for the uncertain noise of the INS [17]. However, these approaches require rigorous training procedures based on a large amount of data to establish the necessary models and thus may not be practical solutions for small UAVs.

To the best of our knowledge, very few studies have investigated the feasibility of robust algorithms for attitude estimation for a small UAV with a minimum number of sensors during a GPS outage. In this paper, we propose a novel robust attitude estimation algorithm for a small UAV with minimal sensors, such as an IMU, a barometer, and an airspeed sensor. In contrast to the aforementioned methods, the proposed method relies on synthetic sideslip angle (SSA) measurements and nongravitational acceleration compensation in combination with a fuzzy adaptive measurement covariance matching algorithm to mitigate the position/velocity drift errors, leading to a higher attitude estimation accuracy. The performance of the proposed method is demonstrated in comparison with the conventional approach and is verified by three different flight tests.

The main contributions of this paper are as follows:

1) A synthetic SSA measurement formulation is first proposed to enhance the attitude estimation for a small UAV without AOA/SSA sensors during a GPS outage.
2) A nongravitational acceleration compensation method based on a Kalman filter is proposed, and a fuzzy-logic-aided measurement covariance matching algorithm is developed to mitigate the effects of disturbed acceleration and magnetic field measurements.
3) The proposed fuzzy adaptive error-state Kalman filter (FAESKF) algorithm is able to use estimated wind states in combination with airspeed measurements and synthetic SSA measurements to extend the dead-reckoning time available when GPS signal blockage occurs in flight.
4) The proposed FAESKF algorithm is verified through experimental flight tests. The validity of the synthetic SSA measurement formulation, the nongravitational acceleration compensation method, and the fuzzy inference system is analyzed in detail.

This paper is organized as follows. The error-state Kalman filter (ESKF), including the sensor modeling and system equation, is presented in Section II. In Section III, the proposed measurement models are formulated. In Section IV, the fuzzy-logic-aided robust estimation algorithm is introduced. The experimental setup and scenarios are briefly summarized in Section V. The results and discussion are presented in Section VI. Conclusions and future work are discussed in Section VII.

II. Error-State Kalman Filter for State Estimation

An arbitrary orientation can be represented by a unit quaternion as follows:

$$\mathbf{q} = q_w + q_x\mathbf{i} + q_y\mathbf{j} + q_z\mathbf{k} = \begin{bmatrix} q_w \\ \mathbf{q}_v \end{bmatrix} = \begin{bmatrix} \cos(\theta/2) \\ \mathbf{e}_x\sin(\theta/2) \\ \mathbf{e}_y\sin(\theta/2) \\ \mathbf{e}_z\sin(\theta/2) \end{bmatrix}$$

where q_w is referred to as the real part of the quaternion and $\mathbf{q}_v = q_x i + q_y j + q_z k$ is the vector part. θ is the rotation angle, and $\bar{\mathbf{e}} = [\mathbf{e}_x,\ \mathbf{e}_y,\ \mathbf{e}_z]^T$ is the axis of rotation. Note that Hamilton's quaternion convention, rather than the JPL quaternion convention, is used in this paper [18].

The successive quaternion product operation is defined as

$$\mathbf{p} \otimes \mathbf{q} = \begin{bmatrix} p_w q_w - \mathbf{p}_v{}^T\mathbf{q}_v \\ p_w\mathbf{q}_v + q_w\mathbf{p}_v + \mathbf{p}_v \times \mathbf{q}_v \end{bmatrix}$$

$$\mathbf{q} \otimes \mathbf{q}^{-\mathbf{1}} = [1,\ 0\,,0\,,\ 0]^T$$

where $\otimes$ denotes quaternion multiplication and $\mathbf{q}^{-\mathbf{1}} = [q_w, -\mathbf{q}_v]^T$ is the inverse quaternion of $\mathbf{q}$.

The quaternion must satisfy the following norm constraint [11]:

$$|\mathbf{q}| = \sqrt{\mathbf{q} \otimes \mathbf{q}^{-1}} = \sqrt{q_w^2 + q_x^2 + q_y^2 + q_z^2} = 1. \qquad (1)$$

The reference frame of the strapdown IMU is called the body-fixed frame $\{b\}$. The navigation frame is denoted by $\{n\}$. In this paper, the local North-East-Down (NED) frame is used as the navigation frame. Hence, an arbitrary 3-dimensional vector $\mathbf{v}^b$ in the body-fixed frame can be transformed into a vector $\mathbf{v}^n$ in the navigation frame as follows [11]:

$$\mathbf{v}^n = \mathbf{R}_b^n(\mathbf{q})\mathbf{v}^b$$

where the rotation matrix $\mathbf{R}_b^n(\mathbf{q}) \in$ SO(3) denotes the relative orientation with respect to the inertial frame as follows:

$$\mathbf{R}_b^n(\mathbf{q}) = \begin{bmatrix} {q_w}^2 + {q_x}^2 - {q_y}^2 - {q_z}^2 & 2(q_x \cdot q_y - q_w \cdot q_z) \\ 2(q_x \cdot q_y + q_w \cdot q_z) & {q_w}^2 - {q_x}^2 + {q_y}^2 - {q_z}^2 \\ 2(q_x \cdot q_z - q_w \cdot q_y) & 2(q_y \cdot q_z + q_w \cdot q_x) \end{bmatrix}$$

$$\begin{bmatrix} 2(q_x \cdot q_z - q_w \cdot q_y) \\ 2(q_y \cdot q_z - q_w \cdot q_x) \\ {q_w}^2 - {q_x}^2 - {q_y}^2 - {q_z}^2 \end{bmatrix}.$$

1558-1748 (c) 2019 IEEE. Personal use is permitted, but republication/redistribution requires IEEE permission. See http://www.ieee.org/publications_standards/publications/rights/index.html for more information.

This article has been accepted for publication in a future issue of this journal, but has not been fully edited. Content may change prior to final publication. Citation information: DOI 10.1109/JSEN.2019.2947489, IEEE Sensors Journal

The conversion between the Euler angles $[\phi,\ \theta,\ \psi]^T$ and the corresponding quaternion can be summarized as follows:

$$\mathbf{q} = \begin{bmatrix} \cos(\phi/2)\cos(\theta/2)\cos(\psi/2) + \sin(\phi/2)\sin(\theta/2)\sin(\psi/2) \\ \sin(\phi/2)\cos(\theta/2)\cos(\psi/2) - \cos(\phi/2)\sin(\theta/2)\sin(\psi/2) \\ \cos(\phi/2)\sin(\theta/2)\cos(\psi/2) + \sin(\phi/2)\cos(\theta/2)\sin(\psi/2) \\ \cos(\phi/2)\cos(\theta/2)\sin(\psi/2) - \sin(\phi/2)\sin(\theta/2)\cos(\psi/2) \end{bmatrix}$$

$$\begin{bmatrix} \phi \\ \theta \\ \psi \end{bmatrix} = \begin{bmatrix} \text{atan2}\left(\frac{2(q_w q_x + q_y q_z)}{1-2(q_x^2+q_y^2)}\right) \\ \text{asin}\left(2(q_w q_y - q_z q_x)\right) \\ \text{atan2}\left(\frac{2(q_w q_z + q_x q_y)}{1-2(q_y^2+q_z^2)}\right) \end{bmatrix}.$$

A. Problem Formulation

Consider the following discrete nonlinear system and measurement models:

$$\mathbf{x}_k \ = \ f(\,\mathbf{x}_{k-1}\,,\,\mathbf{u}_k,\ \mathbf{w}_k)$$
$$\mathbf{z}_k \ = \ h(\mathbf{x}_k\,,\,\mathbf{v}_k)$$

where k is the time index, $\mathbf{x}_k$ the state, $\mathbf{u}_k$ the input, and $\mathbf{z}_k$ the measurement, $f\,(\cdot)$ and $h\,(\cdot)$, the system and measurement models, respectively. The system noise and measurement noise are generally considered to be white Gaussian noise, such that $\mathbf{w}_k \sim N(0, \mathbf{Q}_k)$ and $\mathbf{v}_k \sim N(0, \mathbf{R}_k)$, where $N(\boldsymbol{\mu}_k, \sum_k)$ denotes a normal distribution with a mean of $\boldsymbol{\mu}_k$ and a covariance of $\sum_k$.

Compared with a direct quaternion-based Kalman filter, the ESKF approach has several distinct benefits. The error-state system usually predicts the small variations around the nominal system equation, thus guaranteeing the validity of linearization [19]. The ESKF approaches will result in convergence to the true attitude from a large estimation error or initialization error and can be regarded as a more robust filter if tuned properly [19]. Moreover, the ESKF approach allows the quaternion to be handled in its minimal representation [20]. Thus, an ESKF based on the IMU equation model is used as the basis for the navigation filter proposed in this paper.

The main principle of an ESKF is to regard the true state ($\mathbf{x}_t$) as a combination of the nominal state ($\mathbf{x}$) and an error state ($\delta\mathbf{x}$), where the error state denotes the difference between the nominal state and the true state, thus yielding the following relationship [21]:

$$\mathbf{x}_t = \mathbf{x} \oplus \delta\mathbf{x} \tag{2}$$

where $\oplus$ denotes the typical addition operation for all state variables $\in \mathbb{R}^3$ except the quaternion state. For the quaternion state, the error state is defined in the local frame as follows:

$$\mathbf{q}_t = \mathbf{q} \otimes \delta\mathbf{q} \tag{3}$$

where $\delta\mathbf{q} = [1, \delta\boldsymbol{\theta}/2]^T$ is the orientation error in SO(3) expressed as a unit quaternion [22].

In the following subsections, the state of the ESKF for attitude estimation is represented by a 19-element true-state vector ($\mathbf{x}_t$), a 19-element nominal-state vector ($\mathbf{x}$), and an 18-element error-state vector ($\delta\mathbf{x}$), as follows:

$$\mathbf{x}_t = [\mathbf{q}_t\ \mathbf{v}_t\ \mathbf{p}_t\ \boldsymbol{\omega}_{bt}\ \mathbf{a}_{bt}\ \mathbf{v}_{wt}\ w_{st}]^T \ \in \ \mathbb{R}^{19} \tag{4a}$$
$$\mathbf{x} = [\mathbf{q}\ \ \mathbf{v}\ \mathbf{p}\ \boldsymbol{\omega}_b\ \mathbf{a}_b\ \mathbf{v}_w\ w_s]^T \ \in \ \mathbb{R}^{19} \tag{4b}$$
$$\delta\mathbf{x} = [\delta\boldsymbol{\theta}\ \ \delta\mathbf{v}\ \delta\mathbf{p}\ \delta\boldsymbol{\omega}_b\ \delta\mathbf{a}_b\ \delta\mathbf{v}_w\ \delta w_s]^T \ \in \ \mathbb{R}^{18} \tag{4c}$$

where $\{q_w, q_x, q_y, q_z\} \in \mathbf{q}$, $\{v_n, v_e, v_d\} \in \mathbf{v}$, and $\{p_n, p_e, p_d\} \in \mathbf{p}$ are the quaternion, velocity, and position, respectively, expressed in the navigation frame; $\{\omega_{bx}, \omega_{by}, \omega_{bz}\} \in \boldsymbol{\omega}_b$ and $\{a_{bx}, a_{by}, a_{bz}\} \in \mathbf{a}_b$ are the gyroscope and accelerometer biases, respectively, in the body-fixed frame; $\{v_{wn}, v_{we}\} \in \mathbf{v}_w$ are the north and east components of the wind state in the navigation frame; and w_s is the scaling factor for the wind state.

A typical IMU measures the accelerations along three axes, the angular rates about three axes, and the magnetic fields along three axes with respect to the body-fixed frame. The measurements produced by the IMU are corrupted by white Gaussian noise and slowly-varying bias terms. The following model represents the relationship between the signals measured by the IMU and the true values. It should be noted that the effects of misalignment and scaling factor error for the IMU are neglected since the effects of these parameters can be minimized through proper calibration.

1) Gyroscope: The three-axis gyroscope measures the angular rate about each of the three axes as follows [23]:

$$\boldsymbol{\omega}_m \ = \ \boldsymbol{\omega}_t \ + \ \boldsymbol{\omega}_{bt} \ + \ \boldsymbol{\omega}_n \tag{5}$$

where $\boldsymbol{\omega}_m \in \mathbb{R}^3$ is the measured angular rate signal, $\boldsymbol{\omega}_t \in \mathbb{R}^3$ the true angular rate signal, $\boldsymbol{\omega}_{bt} \in \mathbb{R}^3$ the slowly varying bias term of the gyroscope, and $\boldsymbol{\omega}_n \in \mathbb{R}^3$ zero-mean Gaussian noise.

2) Accelerometer: The accelerometer measures the acceleration signal as follows [24]:

$$\begin{aligned} \mathbf{a}_m &= \mathbf{R}_b^n(\mathbf{q})^T(\mathbf{a}_t - \mathbf{g}) \ + \ \mathbf{a}_{bt} \ + \ \mathbf{a}_n \\ &= \dot{\mathbf{v}}^b + \boldsymbol{\omega} \times \mathbf{v}^b - \mathbf{R}_n^b(\mathbf{q})\mathbf{g} + \ \mathbf{a}_{bt} \ + \ \mathbf{a}_n \end{aligned} \tag{6}$$

where $\mathbf{a}_m \in \mathbb{R}^3$ is the measured acceleration, $\mathbf{v}^b \in \mathbb{R}^3$ the translational velocity vector in the body-fixed frame, $\mathbf{g} \in \mathbb{R}^3$ the gravitational acceleration in the navigation frame, $\mathbf{a}_{bt} \in \mathbb{R}^3$ the slowly varying bias term for the accelerometer, and $\mathbf{a}_n \sim N(0, \sigma_{\mathbf{a}}^2)$ zero-mean Gaussian noise.

In stationary or low-dynamics conditions such as level-flight condition ($\dot{\mathbf{v}}^b,\ \boldsymbol{\omega} \approx 0$), the measured acceleration from (6) can be approximated as follows [23]:

$$\mathbf{a}_m = \begin{bmatrix} a_{mx} \\ a_{my} \\ a_{mz} \end{bmatrix} \approx -\mathbf{R}_n^b(\mathbf{q})\mathbf{g} = \begin{bmatrix} |\mathbf{g}|\ \sin\theta \\ -|\mathbf{g}|\ \sin\phi\ \cos\theta \\ -|\mathbf{g}|\ \cos\phi\ \cos\theta \end{bmatrix}.$$

Thus, in stationary condition, the accelerometer can be used as a tilt sensor, and the roll (ϕ) and pitch (θ) angles can be obtained via the following equations:

$$\begin{bmatrix} \phi \\ \theta \end{bmatrix} = \begin{bmatrix} \text{atan2}\left(\frac{a_{my}}{a_{mz}}\right) \\ \text{atan2}\left(\frac{a_{mx}}{\sqrt{{a_{my}}^2 + {a_{mz}}^2}}\right) \end{bmatrix}.$$

However, (6) does not hold under accelerative motion of the UAV. Thus, the nongravitational acceleration should be estimated to correct the accelerometer measurement when the UAV is accelerating.

1558-1748 (c) 2019 IEEE. Personal use is permitted, but republication/redistribution requires IEEE permission. See http://www.ieee.org/publications_standards/publications/rights/index.html for more information.

This article has been accepted for publication in a future issue of this journal, but has not been fully edited. Content may change prior to final publication. Citation information: DOI 10.1109/JSEN.2019.2947489, IEEE Sensors Journal

3) Wind States: The typical wind states under moderate weather conditions generally consist of constant wind, gusts, and turbulent flows that can nevertheless be approximated as constant over a certain period of flight time [25]. Thus, constant 2-dimensional wind conditions are assumed, and the wind-state variables consist of the north and east components $\{v_{wn,t}, v_{we,t}\} \in \mathbf{v}_{wt}$ and a wind-state scaling factor w_{st}. These three state variables are modeled as random-walk processes as follows [25]:

$$\begin{bmatrix} \dot{\mathbf{v}}_{wt} \\ \dot{w}_{st} \end{bmatrix} = \begin{bmatrix} \mathbf{v}_w \\ w_s \end{bmatrix} \tag{7}$$

where $\mathbf{v}_w$ and w_s represent white Gaussian driving noise.

B. System Equation

In the ESKF formulation, the true-state, nominal-state, and error-state equation are addressed. The true system equation, including noise, can be represented as follows [39]:

$$\dot{\mathbf{x}}_t = \begin{bmatrix} \dot{\mathbf{q}}_t \\ \dot{\mathbf{v}}_t \\ \dot{\mathbf{p}}_t \\ \dot{\boldsymbol{\omega}}_{bt} \\ \dot{\mathbf{a}}_{bt} \\ \dot{\mathbf{v}}_{wt} \\ \dot{w}_{st} \end{bmatrix} = \begin{bmatrix} \frac{1}{2}\mathbf{q}_t \otimes (\boldsymbol{\omega}_m - \boldsymbol{\omega}_{bt} - \boldsymbol{\omega}_n) \\ \mathbf{R}^n_{b,t}(\mathbf{a}_m - \mathbf{a}_{bt} - \mathbf{a}_n) + \mathbf{g} \\ \mathbf{v}_t \\ \boldsymbol{\omega}_\omega \\ \mathbf{a}_\omega \\ \mathbf{v}_w \\ w_s \end{bmatrix} \tag{8}$$

where $\boldsymbol{\omega}_w$ and $\mathbf{a}_w$ represent random-walk noise in the gyroscope and accelerometer biases. The detailed noise statistics will be addressed in the following subsections.

The nominal system model represents the system dynamics in the absence of noise and perturbations and can be represented as follows:

$$\dot{\mathbf{x}} = \begin{bmatrix} \dot{\mathbf{q}} \\ \dot{\mathbf{v}} \\ \dot{\mathbf{p}} \\ \dot{\boldsymbol{\omega}}_b \\ \dot{\mathbf{a}}_b \\ \dot{\mathbf{v}}_w \\ \dot{w}_s \end{bmatrix} = \begin{bmatrix} \frac{1}{2}\mathbf{q} \otimes (\boldsymbol{\omega}_m - \boldsymbol{\omega}_b) \\ \mathbf{R}^n_b(\mathbf{a}_m - \mathbf{a}_b) + \mathbf{g} \\ \mathbf{v} \\ 0_{3\times1} \\ 0_{3\times1} \\ 0_{2\times1} \\ 0_{1\times1} \end{bmatrix}. \tag{9}$$

To obtain the linearized error dynamics, each true-state equation in (8) is reformulated as the corresponding combination of the nominal and error states based on (9) and is simplified up to all second-order infinitesimals, yielding the following error-state equation:

$$\delta\dot{\mathbf{x}} = \begin{bmatrix} \delta\dot{\boldsymbol{\theta}} \\ \delta\dot{\mathbf{v}} \\ \delta\dot{\mathbf{p}} \\ \delta\dot{\boldsymbol{\omega}}_b \\ \delta\dot{\mathbf{a}}_b \\ \delta\dot{\mathbf{v}}_w \\ \delta\dot{w}_s \end{bmatrix} = \begin{bmatrix} -[\boldsymbol{\omega}_m - \boldsymbol{\omega}_b]_\times \delta\boldsymbol{\theta} \; - \; \delta\boldsymbol{\omega}_b \; - \; \boldsymbol{\omega}_n \\ -\mathbf{R}^n_b[\mathbf{a}_m - \mathbf{a}_b]_\times \delta\boldsymbol{\theta} \; - \; \mathbf{R}^n_b \delta\mathbf{a}_b \; - \; \mathbf{R}^n_b \mathbf{a}_n \\ \delta\mathbf{v} \\ \boldsymbol{\omega}_{\boldsymbol{\omega}} \\ \mathbf{a}_\omega \\ \mathbf{v}_w \\ w_w \end{bmatrix} \tag{10}$$

where

$$[\mathbf{a}]_\times = \begin{bmatrix} 0 & -a_z & a_y \\ a_z & 0 & -a_x \\ -a_y & a_x & 0 \end{bmatrix}.$$

C. Error-State Kalman Filter Formulation

The nominal state does not include the noise term in (8) and is propagated by integrating the nominal equation (9) as follows:

$$\hat{\mathbf{x}}^-_k \; = \; f(\hat{\mathbf{x}}^+_{k-1}, \, \mathbf{u}_{k-1}, 0) \tag{11}$$

where $\mathbf{u}_k = [\mathbf{a}_m, \; \boldsymbol{\omega}_m]^{\,T}$ and the superscripts $+$ and $-$ refer to the a posteriori and a priori estimates, respectively. The corresponding nominal-state vector equation is represented as follows:

$$\hat{\mathbf{x}}^-_k = \begin{bmatrix} \hat{\mathbf{q}}^-_k \\ \hat{\mathbf{v}}^-_k \\ \hat{\mathbf{p}}^-_k \\ \hat{\boldsymbol{\omega}}^-_{b,k} \\ \hat{\mathbf{a}}^-_{b,k} \\ \hat{\mathbf{v}}^-_{w,k} \\ \hat{w}^-_{s,k} \end{bmatrix} = \begin{bmatrix} \hat{\mathbf{q}}^+_{k-1} \otimes \mathbf{q}\{(\boldsymbol{\omega}_m - \boldsymbol{\omega}_b)\Delta t\} \\ \hat{\mathbf{v}}^+_{k-1} + (\mathbf{R}^n_b(\mathbf{a}_m - \mathbf{a}_b) + \mathbf{g})\,\Delta t \\ \hat{\mathbf{p}}^+_{k-1} + \hat{\mathbf{v}}^-_k \Delta t \\ \hat{\boldsymbol{\omega}}^+_{b,k-1} \\ \hat{\mathbf{a}}^+_{b,k-1} \\ \hat{\mathbf{v}}^+_{w,k-1} \\ \hat{w}^+_{s,k-1} \end{bmatrix} \tag{12}$$

where Δt is the sampling rate of the IMU and has an almost constant value. Linear evolution of $\boldsymbol{\omega}$ during Δt is assumed; then, the first-order quaternion integrator can be implemented as follows [20]:

$$\hat{\mathbf{q}}^-_k = \hat{\mathbf{q}}^+_{k-1} \otimes \left(\mathbf{q}(\bar{\boldsymbol{\omega}}\Delta t) + \frac{\Delta t^2}{24} \begin{bmatrix} 0 \\ \boldsymbol{\omega}_{k-1} \times \boldsymbol{\omega}_k \end{bmatrix} \right)$$

where $\bar{\boldsymbol{\omega}} = 0.5(\boldsymbol{\omega}_k + \boldsymbol{\omega}_{k-1})$ is the average angular rate during time steps $k-1$ and k.

The integration of the error-state equation in (10) yields the following:

$$\delta\hat{\mathbf{x}}^-_k \; = \; \mathbf{F}\,\delta\hat{\mathbf{x}}^+_{k-1} \tag{13}$$

where $\mathbf{F}$ is the transition matrix and can be obtained via Euler integration of (10) with respect to the error state $\delta\mathbf{x}$ as follows [21]:

$$\mathbf{F} \cong \mathbf{I} \; + \mathbf{A}\Delta t$$

where $\mathbf{F}$ is approximated by only the first-order term since the sampling time Δt is extremely short.

$$\mathbf{A} = \partial f(x,\cdot)/\partial\delta\mathbf{x}$$
$$= \begin{bmatrix} \Theta & 0_{3\times3} & 0_{3\times3} & -\mathrm{I}_{3\times3} & 0_{3\times3} & 0_{3\times2} & 0_{3\times1} \\ \mathbf{V} & 0_{3\times3} & 0_{3\times3} & 0_{3\times3} & -\mathbf{R}^n_b & 0_{3\times2} & 0_{3\times1} \\ 0_{3\times3} & \mathrm{I}_{3\times3} & 0_{3\times3} & 0_{3\times3} & 0_{3\times3} & 0_{3\times2} & 0_{3\times1} \\ 0_{3\times3} & 0_{3\times3} & 0_{3\times3} & 0_{3\times3} & 0_{3\times3} & 0_{3\times2} & 0_{3\times1} \\ 0_{3\times3} & 0_{3\times3} & 0_{3\times3} & 0_{3\times3} & 0_{3\times3} & 0_{3\times2} & 0_{3\times1} \\ 0_{2\times3} & 0_{2\times3} & 0_{2\times3} & 0_{2\times3} & 0_{2\times3} & 0_{2\times2} & 0_{2\times1} \\ 0_{1\times3} & 0_{1\times3} & 0_{1\times3} & 0_{1\times3} & 0_{1\times3} & 0_{1\times2} & 0_{1\times1} \end{bmatrix}$$

where

$$\Theta \; = \; -[\boldsymbol{\omega}_m - \boldsymbol{\omega}_b]_\times, \;\; \mathbf{V} \; = \; -\mathbf{R}^n_b[\mathbf{a}_m - \mathbf{a}_b]_\times.$$

Generally, the prediction step represented by (13) for the error state $\delta\hat{\mathbf{x}}_k$ can be neglected because the initial value of the error state $\delta\hat{\mathbf{x}}_k$ is set to zero. The a priori covariance $\mathbf{P}^-_k$ is updated as follows:

$$\mathbf{P}^-_k \; = \; \mathbf{F}\,\mathbf{P}^+_{k-1}\,\mathbf{F}^T \; + \; \mathbf{F}_i\,\mathbf{Q}_i\,\mathbf{F}^T_i \tag{14}$$

1558-1748 (c) 2019 IEEE. Personal use is permitted, but republication/redistribution requires IEEE permission. See http://www.ieee.org/publications_standards/publications/rights/index.html for more information.

This article has been accepted for publication in a future issue of this journal, but has not been fully edited. Content may change prior to final publication. Citation information: DOI 10.1109/JSEN.2019.2947489, IEEE Sensors Journal

where $\mathbf{F}_i$ is the perturbed Jacobian of (10) with respect to the perturbation vector i, as follows:

$$\mathbf{F}_i = \partial f(x,\cdot)/\partial \delta \mathbf{w} = \begin{bmatrix} -\mathrm{I}_{3\times3} & 0_{3\times3} & 0_{3\times3} & 0_{3\times3} & 0_{3\times3} & 0_{3\times2} & 0_{3\times1} \\ 0_{3\times3} & -\mathrm{I}_{3\times3} & 0_{3\times3} & 0_{3\times3} & 0_{3\times3} & 0_{3\times2} & 0_{3\times1} \\ 0_{3\times3} & 0_{3\times3} & 0_{3\times3} & 0_{3\times3} & 0_{3\times3} & 0_{3\times2} & 0_{3\times1} \\ 0_{3\times3} & 0_{3\times3} & 0_{3\times3} & \mathrm{I}_{3\times3} & 0_{3\times3} & 0_{3\times2} & 0_{3\times1} \\ 0_{3\times3} & 0_{3\times3} & 0_{3\times3} & 0_{3\times3} & \mathrm{I}_{3\times3} & 0_{3\times2} & 0_{3\times1} \\ 0_{2\times3} & 0_{2\times3} & 0_{2\times3} & 0_{2\times3} & 0_{2\times3} & \mathrm{I}_{2\times2} & 0_{2\times1} \\ 0_{1\times3} & 0_{1\times3} & 0_{1\times3} & 0_{1\times3} & 0_{1\times3} & 0_{1\times2} & \mathrm{I}_{1\times1} \end{bmatrix}$$

where $\mathbf{w} = [\boldsymbol{\omega}_n \ \mathbf{a}_n \ \boldsymbol{\omega}_\omega \ \mathbf{a}_\omega \ \mathbf{v}_w \ w_w]^T$, and $\mathbf{Q}_i$ is the covariance matrix of the perturbation impulses, given by

$$\mathbf{Q}_i = \begin{bmatrix} \Upsilon_i & 0_{3\times3} & 0_{3\times3} & 0_{3\times3} & 0_{3\times2} & 0_{3\times1} \\ 0_{3\times3} & \mathbf{V}_i & 0_{3\times3} & 0_{3\times3} & 0_{3\times2} & 0_{3\times1} \\ 0_{3\times3} & 0_{3\times3} & \Omega_i & 0_{3\times3} & 0_{3\times2} & 0_{3\times1} \\ 0_{3\times3} & 0_{3\times3} & 0_{3\times3} & \Psi_i & 0_{3\times2} & 0_{3\times1} \\ 0_{2\times3} & 0_{2\times3} & 0_{2\times3} & 0_{2\times3} & \mathbf{V}_{w,i} & 0_{2\times1} \\ 0_{1\times3} & 0_{1\times3} & 0_{1\times3} & 0_{1\times3} & 0_{1\times2} & \mathbf{W}_{s,i} \end{bmatrix} \tag{15}$$

where

$$\begin{aligned} \Upsilon_i &= \sigma^2_{\boldsymbol{\omega}_n} \Delta t^2 \, \mathrm{I}_{3\times3} && [\mathrm{rad}^2] \\ \mathbf{V}_i &= \sigma^2_{\mathbf{a}_n} \Delta t^2 \, \mathrm{I}_{3\times3} && [\mathrm{m}^2/\mathrm{s}^2] \\ \Omega_i &= \sigma^2_{\boldsymbol{\omega}_\omega} \Delta t \, \mathrm{I}_{3\times3} && [\mathrm{rad}^2/\mathrm{s}^2] \\ \Psi_i &= \sigma^2_{\mathbf{a}_\omega} \Delta t \, \mathrm{I}_{3\times3} && [\mathrm{m}^2/\mathrm{s}^4] \\ \mathbf{V}_{w,i} &= \sigma^2_{\mathbf{v}_w} \Delta t \, \mathrm{I}_{2\times2} && [\mathrm{m}^2/\mathrm{s}^2] \\ \mathbf{W}_{s,i} &= \sigma^2_{w_w} \Delta t \, \mathrm{I}_{1\times1} && [\text{dimensionless}] \end{aligned}$$

where $\sigma_{\boldsymbol{\omega}_n}[\mathrm{rad/s}]$, $\sigma_{\mathbf{a}_n}[\mathrm{m/s}^2]$, $\sigma_{\boldsymbol{\omega}_\omega}[\mathrm{rad/s}/\sqrt{\mathrm{s}}]$, and $\sigma_{\mathbf{a}_\omega}[\mathrm{m/s}^2/\sqrt{\mathrm{s}}]$ can be determined from the information given in the IMU's specifications or through Allan variance analysis [27] and $\sigma_{\mathbf{v}_w}$ $[\mathrm{m/s}^2/\sqrt{\mathrm{s}}]$ and σ_{w_w} [dimensionless] must be determined through trial-and-error-based tuning.

A measurement update of the ESKF will be executed whenever valid measurements are available. The Kalman gain of the ESKF, $\mathbf{K}_k$, is calculated as follows [20]:

$$\mathbf{K}_k = \mathbf{P}_k^- {\mathbf{H}_k}^T (\mathbf{H}_k \mathbf{P}_k^- {\mathbf{H}_k}^T + \mathbf{R}_k)^{-1} \tag{16}$$

where

$$\mathbf{H}_k = \left.\frac{\partial h}{\partial \delta \mathbf{x}}\right|_{\mathbf{x}} = \left.\frac{\partial h}{\partial \mathbf{x}_t}\right|_{\mathbf{x}} \left.\frac{\partial \mathbf{x}_t}{\partial \delta \mathbf{x}}\right|_{\mathbf{x}} = \mathbf{H}_{\mathbf{x}} \mathbf{X}_{\delta \mathbf{x}},$$

$$\mathbf{X}_{\delta x} = \begin{bmatrix} \mathbf{Q}_{\delta\boldsymbol{\theta}} & 0 \\ 0 & \mathrm{I}_{15\times16} \end{bmatrix},$$

and

$$\mathbf{Q}_{\delta\boldsymbol{\theta}} = \frac{\partial(\mathbf{q}\otimes\delta\mathbf{q})}{\partial\delta\boldsymbol{\theta}} = \left.\frac{\partial(\mathbf{q}\otimes\delta\mathbf{q})}{\partial\delta\mathbf{q}}\right|_{\mathbf{q}} \left.\frac{\partial\delta\mathbf{q}}{\partial\delta\boldsymbol{\theta}}\right|_{\delta\hat{\boldsymbol{\theta}}=0}$$

$$= \left.\frac{\partial([\mathbf{q}]_L\delta\mathbf{q})}{\partial\delta\mathbf{q}}\right|_{\mathbf{q}} \left.\frac{\partial\begin{bmatrix}1\\ \frac{1}{2}\delta\boldsymbol{\theta}\end{bmatrix}}{\partial\delta\boldsymbol{\theta}}\right|_{\delta\hat{\boldsymbol{\theta}}=0} = [\mathbf{q}]_L \frac{1}{2} \begin{bmatrix} 0&0&0 \\ 1&0&0 \\ 0&1&0 \\ 0&0&1 \end{bmatrix}$$

where $[\mathbf{q}]_L$ denotes the left-quaternion-product matrix as follows:

$$[\mathbf{q}]_L = \begin{bmatrix} q_w & -q_x & -q_y & -q_z \\ q_x & q_w & -q_z & q_y \\ q_y & q_z & q_w & -q_x \\ q_z & -q_y & q_x & q_w \end{bmatrix}.$$

The a posteriori estimate of the error state, $\delta\hat{\mathbf{x}}_k^+$, and the a posteriori covariance, $\mathbf{P}_k^+$, are updated as follows:

$$\delta\hat{\mathbf{x}}_k^+ = \mathbf{K}_k \boldsymbol{\nu}_k \tag{17}$$

where $\boldsymbol{\nu}_k = \mathbf{z}_k - h(\hat{\mathbf{x}}_k^-)$ denotes the innovation sequence at time k, and

$$\mathbf{P}_k^+ = (\mathbf{I} - \mathbf{K}_k \mathbf{H}_k)\, \mathbf{P}_k^-. \tag{18}$$

After the completion of the measurement update of the ESKF, the nominal state is updated using the a posteriori error state via the following operation:

$$\hat{\mathbf{x}}_k^+ \leftarrow \hat{\mathbf{x}}_k^- \oplus \delta\hat{\mathbf{x}}_k^+ \tag{19}$$

In detail, the update of the corresponding nominal state using the a posteriori error state is represented as follows:

$$\hat{\mathbf{x}}_k^+ = \begin{bmatrix} \hat{\mathbf{q}}_k^+ \\ \hat{\mathbf{v}}_k^+ \\ \hat{\mathbf{p}}_k^+ \\ \hat{\boldsymbol{\omega}}_{b,k}^+ \\ \hat{\mathbf{a}}_{b,k}^+ \\ \hat{\mathbf{v}}_{w,k}^+ \\ \hat{w}_{s,k}^+ \end{bmatrix} = \begin{bmatrix} \hat{\mathbf{q}}_k^- \otimes q\{\delta\hat{\boldsymbol{\theta}}_k^+\} \\ \hat{\mathbf{v}}_k^- + \delta\hat{\mathbf{v}}_k^+ \\ \hat{\mathbf{p}}_k^- + \delta\hat{\mathbf{p}}_k^+ \\ \hat{\boldsymbol{\omega}}_{b,k}^- + \delta\hat{\boldsymbol{\omega}}_k^+ \\ \hat{\mathbf{a}}_{b,k}^- + \delta\hat{\mathbf{a}}_k^+ \\ \hat{\mathbf{v}}_{w,k}^- + \delta\hat{\mathbf{v}}_{w,k}^+ \\ \hat{w}_{s,k}^- + \delta\hat{w}_{s,k}^+ \end{bmatrix}. \tag{20}$$

After the update of the nominal state with the error state, the mean of the error state $\delta\hat{\mathbf{x}}_k^+$ is reset to zero, and the a posteriori covariance must be updated in accordance with this modification [21]:

$$\mathbf{P}_k^+ = \mathbf{G}_k \, \mathbf{P}_k^+ \, \mathbf{G}_k^T \tag{21}$$

where

$$\mathbf{G}_k = \left.\frac{\partial g}{\partial \delta\mathbf{x}}\right|_{\delta\hat{\mathbf{x}}^+} = \begin{bmatrix} \mathbf{I} - \left[\frac{1}{2}\delta\hat{\boldsymbol{\theta}}_k^+\right]_\times & 0 \\ 0 & \mathbf{I}_{15\times15} \end{bmatrix}.$$

It should be noted that after the operation expressed in (20), the quaternion normalization constraint shown in (1) can be violated due to the linearization and arithmetic errors. To prevent such a case, a brute-force quaternion normalization operation should be executed if the discrepancy from the unit norm is larger than a small fraction of the noise level ϵ (i.e., 10^{-7}) [28]:

$$\hat{\mathbf{q}}_k^+ = \frac{\hat{\mathbf{q}}_k^+}{|\hat{\mathbf{q}}_k^+|} \geq \epsilon. \tag{22}$$

1558-1748 (c) 2019 IEEE. Personal use is permitted, but republication/redistribution requires IEEE permission. See http://www.ieee.org/publications_standards/publications/rights/index.html for more information.

This article has been accepted for publication in a future issue of this journal, but has not been fully edited. Content may change prior to final publication. Citation information: DOI 10.1109/JSEN.2019.2947489, IEEE Sensors Journal

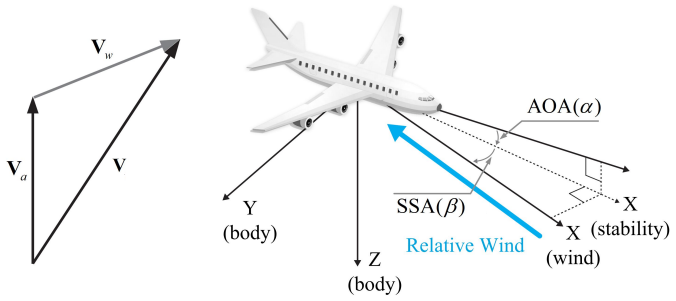


Fig. 1: The wind triangle and the relationship between the AOA, SSA, and true airspeed. $\mathbf{v}$, $\mathbf{v}_a$, and $\mathbf{v}_w$ denote the ground, airspeed, and wind velocities, respectively, in the navigation frame.

III. Measurement Model

The measurements used in the proposed algorithm consist of accelerometer, magnetometer, barometer, airspeed, GPS, and synthetic SSA measurements. Among them, the GPS measurements provide the north and east components of the position information (p_n and p_e, respectively) and the north, east, and down components of the velocity information (v_n, v_e, and v_d, respectively). The barometer measurements provide the down component of the position information, p_d. It should be noted that the GPS measurements are used only to generate ground-truth data. The details of the GPS and barometer measurements are omitted here for simplicity; the measurement formulations for the remaining sensor measurements are the main focus of this paper and thus will be discussed in detail.

A. Synthetic Sideslip Angle Measurements

The geometric relationship between the AOA, SSA, and airspeed is depicted in Fig. 1. By utilizing this geometric relationship, the airspeed $\mathbf{v}_{a,k}$, the AOA α_k, and the SSA β_k at time k can be expressed in the body-fixed frame as follows [29]:

$$\mathbf{v}^b_{a,k} = \begin{bmatrix} u_k \\ v_k \\ w_k \end{bmatrix}_b = \begin{bmatrix} \left|\mathbf{v}^b_{a,k}\right| \cos\alpha_k \cos\beta_k \\ \left|\mathbf{v}^b_{a,k}\right| \sin\beta_k \\ \left|\mathbf{v}^b_{a,k}\right| \sin\alpha_k \cos\beta_k \end{bmatrix}$$

$$\alpha_k = \tan^{-1}\left(\frac{w_k}{u_k}\right)$$

$$\beta_k = \sin^{-1}\left(\frac{v_k}{\left|\mathbf{v}^b_{a,k}\right|}\right)$$

where $\left|\mathbf{v}^b_{a,k}\right| = \sqrt{u_k^2 + v_k^2 + w_k^2}$ is the magnitude of the airspeed [29].

Depending on the flight regime and the characteristics of the aircraft, the AOA and SSA can vary significantly. However, the flight mission trajectory of a small UAV usually does not involve extreme aggressive maneuvers. The variations of the SSA in nonaggressive maneuvers may be neglected and thus can be approximated as zero. By contrast, the AOA of a small UAV can vary considerably depending on the severity of the turning motion. In this paper, by utilizing the small-angle approximation for the SSA, the airspeed is approximated as follows:

$$\mathbf{v}^b_{a,k} \approx \begin{bmatrix} \left|\mathbf{v}^b_{a,k}\right| \cos\alpha_k \\ 0 \\ \left|\mathbf{v}^b_{a,k}\right| \sin\alpha_k \end{bmatrix}.$$

Utilizing the further assumption that $\left|\mathbf{v}^b_{a,k}\right| \approx u_k$, a synthetic SSA measurement $\beta_{s,k}$ is newly formulated as follows:

$$\begin{aligned} \beta_{s,k} &= \sin^{-1}\left(\frac{v_k}{\left|\mathbf{v}^b_{a,k}\right|}\right) \\ &\approx \frac{v_k}{u_k} + \beta_n \end{aligned} \tag{23}$$

where $\beta_n \sim N(0, \sigma_s^2)$ denotes zero-mean white Gaussian noise. The physical interpretation of the synthetic SSA measurement formulation given in (23) indicates that the zero-angle assumption for the SSA is satisfied when the airspeed along the body-fixed x-axis, u_k, has a significantly larger value than the airspeed along the body-fixed y-axis, v_k.

Thus, the corresponding innovation sequence $\nu_{s,k}$ for the synthetic SSA measurements, under the assumption of $\beta_{s,k} \approx 0$, can be expressed as follows:

$$\begin{aligned} \nu_{s,k} &= \overbrace{\beta_{s,k}}^{\text{Synthetic SSA Measurement}} - \overbrace{\frac{\hat{v}_k^-}{\hat{u}_k^-}}^{\text{Predicted Synthetic SSA}} \\ &\approx \overbrace{0}^{\text{Synthetic SSA Measurement}} - \overbrace{\frac{\hat{v}_k^-}{\hat{u}_k^-}}^{\text{Predicted synthetic SSA}} \end{aligned}$$

The zero-angle assumption for the SSA has been used in many previous studies to simplify the formulation of the problem [7], [13], [30], but to our knowledge, this paper may be the first to utilize synthetic SSA measurements under the zero-angle assumption in an estimation filter framework to improve the estimation performance during a GPS outage. The validity of the approximation described above will be analyzed in Section VI.

To formulate the synthetic SSA measurement from the defined states, v_k and u_k in (23) can be obtained, utilizing the wind triangle relationship $\mathbf{v}_k = \mathbf{v}_{a,k} + \mathbf{v}_{w,k}$, as follows:

$$\mathbf{v}^b_{a,k} = \begin{bmatrix} u_k \\ v_k \\ w_k \end{bmatrix}_b = \mathbf{R}^b_n \left(\mathbf{v}_k - \mathbf{v}_{w,k}\right). \tag{24}$$

From (24), it can be deduced that the synthetic SSA measurement provides not only the ground velocity and wind velocity but also attitude information. Thus, to prevent the adverse effect of inaccurate attitude estimation in the synthetic SSA measurement, the chi-square fault detection algorithm is implemented as follows:

$$\varepsilon_k = \left(\mathbf{z}_k - h(\hat{\mathbf{x}}_k^-)\right)^T \mathbf{S}_k^{-1} \left(\mathbf{z}_k - h(\hat{\mathbf{x}}_k^-)\right) \tag{25}$$

1558-1748 (c) 2019 IEEE. Personal use is permitted, but republication/redistribution requires IEEE permission. See http://www.ieee.org/publications_standards/publications/rights/index.html for more information.

This article has been accepted for publication in a future issue of this journal, but has not been fully edited. Content may change prior to final publication. Citation information: DOI 10.1109/JSEN.2019.2947489, IEEE Sensors Journal

where $\mathbf{S}_k = \mathbf{H}_k \mathbf{P}_k^- \mathbf{H}_k^T + \mathbf{R}_k$ refers to the innovation covariance matrix. The statistical hypothesis testing for detecting measurement failure based on the chi-square distribution can be defined as follows:

$$\begin{cases} \varepsilon_k \geq T_{chi} & \text{Measurement fault} \\ \varepsilon_k < T_{chi} & \text{Normal} \end{cases} \tag{26}$$

where T_{chi} can be obtained from the desired confidence level of the chi-square distribution. 95% confidence level was utilized in this paper. If a fault of measurement is detected by (26), then the synthetic SSA measurement is utilized in the measurement update procedure.

B. Airspeed Measurements

Utilizing the wind triangle relationship shown in Fig. 1, the relationship between the velocity $\mathbf{v}_k^b$ and the airspeed $\mathbf{v}_{a,k}^b$ in the body-fixed frame and the wind state $\mathbf{v}_{w,k}$ in the navigation frame at time k can be represented as follows [25]:

$$\mathbf{v}_k^b = \mathbf{v}_{a,k}^b + \mathbf{R}_n^b(\mathbf{q})\mathbf{v}_{w,k}. \tag{27}$$

Rearranging (27) yields

$$\mathbf{v}_{a,k}^b = \begin{bmatrix} u_k \\ v_k \\ w_k \end{bmatrix}_b = \mathbf{R}_n^b(\mathbf{q}) \begin{bmatrix} v_{n,k} \\ v_{e,k} \\ v_{d,k} \end{bmatrix}_n - \mathbf{R}_n^b(\mathbf{q}) \begin{bmatrix} v_{wn,k} \\ v_{we,k} \\ 0 \end{bmatrix}_n . \tag{28}$$

$$\left\|\mathbf{v}_{a,k}^b\right\| = \sqrt{(v_{n,k} - v_{wn,k})^2 + (v_{e,k} - v_{we,k})^2 + (v_{d,k})^2} \tag{29}$$

where $[\cdot]_b$ and $[\cdot]_n$ denote vectors expressed in the body-fixed and navigation frames, respectively.

In terms of the AOA α, the SSA β, and $\mathbf{v}_{a,k}^b$, the pitot-static tube airspeed v_{pitot} can be expressed as follows [29]:

$$v_{pitot} = \mathbf{v}_{a,k}^b \cos\alpha \sin\beta.$$

Utilizing Bernoulli's equation, the airspeed measurement $z_{ar,k}$ is obtained by

$$z_{ar,k} = \frac{\rho}{2} v_{pitot}^2.$$

where ρ denotes the air density. The scale factor $w_{s,k}$ is then defined by

$$w_{s,k} = \frac{\rho}{2} \cos^2\alpha \sin^2\beta.$$

By utilizing (28)-(29), $z_{ar,k}$ can be expressed as follows:

$$z_{ar,k} = w_{s,k}\left[(v_{n,k} - v_{wn,k})^2 + (v_{e,k} - v_{we,k})^2 + (v_{d,k})^2\right] + ar_n \tag{30}$$

where $ar_n \sim N(0, \sigma_{ar}^2)$ denotes zero-mean Gaussian noise.

TABLE I
Fuzzy rules for $\lambda_{\mathbf{a},k}$

ξ_1 \ ξ_2	Minus	Zero	Plus
VS	S	VS	VS
S	S	VS	S
M	M	S	L
L	M	S	L
VL	L	M	VL

TABLE II
Fuzzy rules for $\lambda_{\mathbf{m},k}$

γ_1 \ γ_2	Minus	Zero	Plus
VS	VS	VS	VS
S	S	VS	S
M	M	S	L
L	M	S	L
VL	L	L	VL

C. Nongravitational Acceleration Estimation

The measured acceleration at time k can be categorized into three components: the translational acceleration $\dot{\mathbf{v}}_k^b$, the centripetal acceleration $\boldsymbol{\omega}_k \times \mathbf{v}_k^b$, and the gravitational acceleration $\mathbf{R}_n^b(q)\mathbf{g}$. To extract only the gravitational acceleration $\tilde{\mathbf{a}}_{m,k}$, the translational acceleration ($\dot{\mathbf{v}}_k^b$) and the centripetal acceleration ($\boldsymbol{\omega}_k \times \mathbf{v}_k^b$) at time k should be subtracted from the raw acceleration measurement $\mathbf{a}_{m,k}$ as follows [13]:

$$\tilde{\mathbf{a}}_{m,k} = \mathbf{a}_{m,k} - \mathbf{D}_k^b \tag{31}$$

where

$$\mathbf{D}_k^b = \dot{\mathbf{v}}_k^b - \boldsymbol{\omega}_k \times \mathbf{v}_k^b \tag{32}$$

denotes the nongravitational disturbance at time k.

The second term in (32) can be easily obtained since the velocity $\mathbf{v}_k^b$ in the body-fixed frame and $\boldsymbol{\omega}_k$ are available from (27) and the gyroscope output, respectively. However, the translational acceleration $\dot{\mathbf{v}}_k^b$ cannot be easily computed since the differentiation of $\mathbf{v}_k^b$ may induce an increase in numerical error. During steady/straight and level flight, the translational acceleration $\dot{\mathbf{v}}_k^b$ can be approximated as zero and thus can be neglected. However, the effect of $\dot{\mathbf{v}}_k^b$ on the measured acceleration cannot be neglected in the case of the accelerating/decelerating motion exhibited during climbing and descending.

Thus, in this paper, a simple Kalman filter is implemented to reliably estimate $\dot{\mathbf{v}}_k^b$, where $\mathbf{v}_k^b = [v_{x,k}^b, v_{y,k}^b, v_{z,k}^b]^T$ is treated as an artificial measurement. The system and measurement models can be expressed as follows:

$$\xi_k = \mathbf{A}_k \xi_{k-1} + \boldsymbol{\Gamma}_k$$
$$\eta_k = \mathbf{B}_k \xi_k + \boldsymbol{\Upsilon}_k$$

1558-1748 (c) 2019 IEEE. Personal use is permitted, but republication/redistribution requires IEEE permission. See http://www.ieee.org/publications_standards/publications/rights/index.html for more information.

This article has been accepted for publication in a future issue of this journal, but has not been fully edited. Content may change prior to final publication. Citation information: DOI 10.1109/JSEN.2019.2947489, IEEE Sensors Journal

where

$$\xi_k = \begin{bmatrix} v^b_{x,k} & \dot{v}^b_{x,k} & v^b_{y,k} & \dot{v}^b_{y,k} & v^b_{z,k} & \dot{v}^b_{z,k} \end{bmatrix}^T$$

$$\mathbf{A}_k = \begin{bmatrix} 1 & \Delta t_a & 0 & 0 & 0 & 0 \\ 0 & 1 & 0 & 0 & 0 & 0 \\ 0 & 0 & 1 & \Delta t_a & 0 & 0 \\ 0 & 0 & 0 & 1 & 0 & 0 \\ 0 & 0 & 0 & 0 & 1 & \Delta t_a \\ 0 & 0 & 0 & 0 & 0 & 1 \end{bmatrix}$$

$$\mathbf{B}_k = \begin{bmatrix} 1 & 0 & 0 & 0 & 0 & 0 \\ 0 & 0 & 1 & 0 & 0 & 0 \\ 0 & 0 & 0 & 0 & 1 & 0 \end{bmatrix}$$

where $\mathbf{\Gamma}_k$ and $\mathbf{\Upsilon}_k$ are set to $\mathrm{diag}\left([0.1, 0.5, 0.1, 0.5, 0.1, 0.5]\right)$ and $\mathrm{diag}\left([0.5, 0.5, 0.5]\right)$, respectively, and Δt_a denotes the sampling time interval of the airspeed measurements. Note that $\mathbf{\Gamma}_k$ and $\mathbf{\Upsilon}_k$ are empirically obtained through trial-and-error tuning to cover the uncertainty of the constant acceleration models. The standard Kalman filter is implemented here [25]; thus, the details are omitted for simplicity.

D. Magnetometer

The magnetometer provides magnetic field measurements as follows [31]:

$$\begin{aligned} \mathbf{m}_m &= \mathbf{R}^n_b(\mathbf{q})^T \cdot \mathbf{M} + \mathbf{m}_n \\ &= \mathbf{R}^n_b(\mathbf{q})^T \cdot \begin{bmatrix} |\mathbf{M}| \cos(\varphi_{inc}) \cos(\varphi_{dec}) \\ |\mathbf{M}| \cos(\varphi_{inc}) \sin(\varphi_{dec}) \\ |\mathbf{M}| \sin(\varphi_{inc}) \end{bmatrix} + m_n \end{aligned} \quad (33)$$

where $\mathbf{m}_m \in \mathbb{R}^3$ is the measured magnetic field, $\mathbf{m}_n \sim N(0, \sigma^2_{\mathbf{m}})$ is zero-mean Gaussian noise, $\mathbf{M}$ is the magnetic field vector of the Earth expressed in the navigation frame, $|\mathbf{M}|$ is the magnitude of the magnetic flux density, φ_{inc} is the inclination angle of the Earth's magnetic field, and φ_{dec} is the declination angle [32]. The last three parameters ($|\mathbf{M}|$, φ_{dec}, and φ_{inc}) depend on the geodetic position and time and can be obtained from the database of the World Magnetic Model (WMM) [1].

Magnetic field measurements have primarily been utilized for extracting yaw angle information, but attitude estimation utilizing the Earth's magnetic field has also been implemented for motion tracking [31], spacecraft [33], and aircraft applications [34]. For the scenarios considered in this paper, the values of the Earth's magnetic field vector $\mathbf{M}$ are almost constant in the flight region because the flight area is not extremely wide. Thus, the roll and pitch angles as well as the yaw angle information can be extracted from magnetic field measurements [23].

IV. Robust Attitude Estimation Algorithm

A. Fuzzy-Logic-Based Covariance Matching Algorithm

The estimation performance of the proposed ESKF is highly dependent on the measurement covariance. In this paper, a fuzzy-logic-aided measurement covariance matching algorithm is proposed based on the Mamdani fuzzy inference system [35], [36]. The fuzzy inference algorithm consists of three consecutive procedures, namely, fuzzification, fuzzy reasoning, and defuzzification. Ideally, the magnitude and direction of the compensated gravitational acceleration $\tilde{\mathbf{a}}_m$ should closely match those of the true gravity vector when the nongravitational acceleration is properly subtracted from the raw acceleration measurement [11]. Accordingly, the following parameters are selected as the inputs to the fuzzy inference system to detect the deviation from the gravity vector:

$$\begin{aligned} \xi_1 &= \ \mathrm{acos}\left(\frac{\tilde{\mathbf{a}}_m}{\|\tilde{\mathbf{a}}_m\|} \cdot \frac{\mathbf{g}}{\|\mathbf{g}\|}\right) \\ \xi_2 &= \|\tilde{\mathbf{a}}_m\| - \|\mathbf{g}\| \end{aligned} \quad (34)$$

where ξ_1 and ξ_2 denote the deviations in angle and magnitude, respectively, from the true gravitational acceleration $\mathbf{g}$.

Similarly, the magnitude and dip angle of the magnetic field should remain nearly constant when no external magnetic disturbance is present [37], [38]. Accordingly, the following two parameters are used as the fuzzy inputs for detecting a disturbance in the magnetic measurement:

$$\begin{aligned} \gamma_1 &= \pi/2 - \ \mathrm{acos}\left(n_{\mathbf{a}} \cdot n_{\mathbf{m}}\right) \\ \gamma_2 &= \|\mathbf{m}_m - |\mathbf{M}|\| \ / \ |\mathbf{M}| \end{aligned} \quad (35)$$

where γ_1 and γ_2 denote the normalized magnitude deviation from the true magnetic field and the dip angle, respectively, and $n_{\mathbf{a}}$ and $n_{\mathbf{m}}$ denote the unit vectors of the measured

Algorithm 1 Proposed FAESKF Algorithm

Inputs: $\mathbf{a}_m$, $\boldsymbol{\omega}_m$
Measurements: $\tilde{\mathbf{a}}_m$, $\mathbf{m}_m$, z_{ar}, β_s, p_d
Initialization: $\mathbf{q}_0$, $\mathbf{v}_0$, $\mathbf{p}_0$ $\boldsymbol{\omega}_{b,0}$, $\mathbf{a}_{b,0}$, $\mathbf{v}_{w,0}$, $w_{s,0}$
Time update:
1. Propagate the nominal state via (11)
2. Propagate the error state via (13)
3. Compute the a priori error covariance via (14)

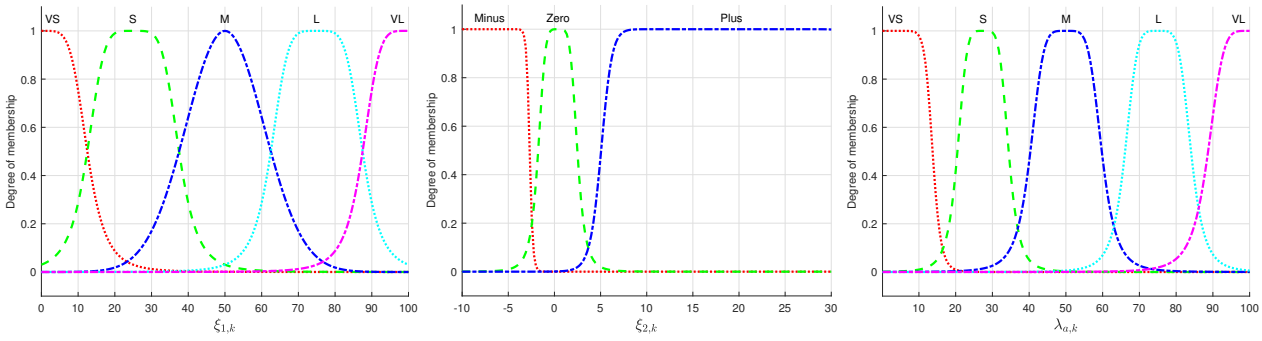
Measurement update:
Acceleration ($\tilde{\mathbf{a}}_m$):
4. Compute the fuzzy input parameters ξ_1 and ξ_2 via (34)
5. Compute the fuzzy output $\lambda_{\mathbf{a},k}$ via Table I
6. Compute the new measurement covariance $\mathbf{R}_{\mathbf{a},k}$ via (36)

Magnetic field ($\mathbf{m}_m$):
7. Compute the fuzzy input parameters γ_1 and γ_2 via (35)
8. Compute the fuzzy output $\lambda_{\mathbf{m},k}$ via Table II
9. Compute the new measurement covariance $\mathbf{R}_{\mathbf{m},k}$ via (36)

Airspeed (z_{ar}):
Barometer (p_d):
Synthetic SSA (β_s):
10. Compute the Kalman gain via (16)
11. Compute the a posteriori error state via (17)
12. Compute the a posteriori error covariance via (18)
13. Update the a posteriori nominal state via (19)
14. Renormalize the quaternion via (22)
15. Update the a posteriori error covariance via (21)

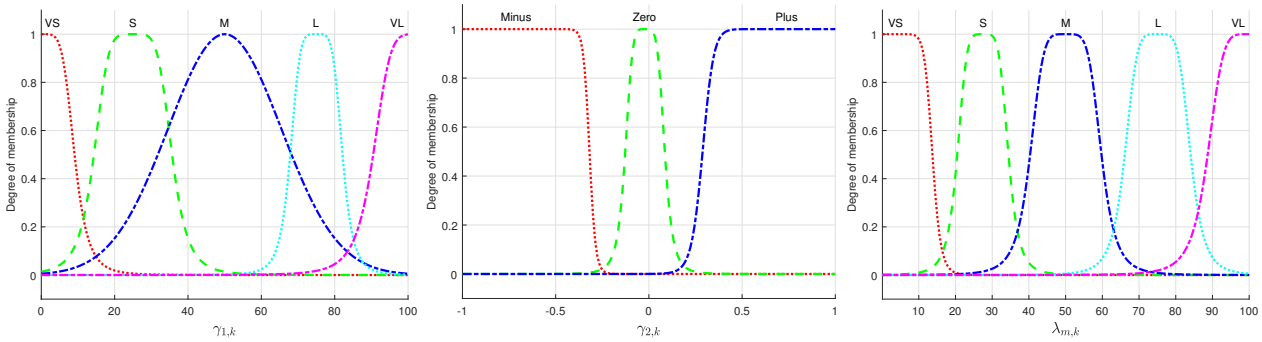
1558-1748 (c) 2019 IEEE. Personal use is permitted, but republication/redistribution requires IEEE permission. See http://www.ieee.org/publications_standards/publications/rights/index.html for more information.

This article has been accepted for publication in a future issue of this journal, but has not been fully edited. Content may change prior to final publication. Citation information: DOI 10.1109/JSEN.2019.2947489, IEEE Sensors Journal



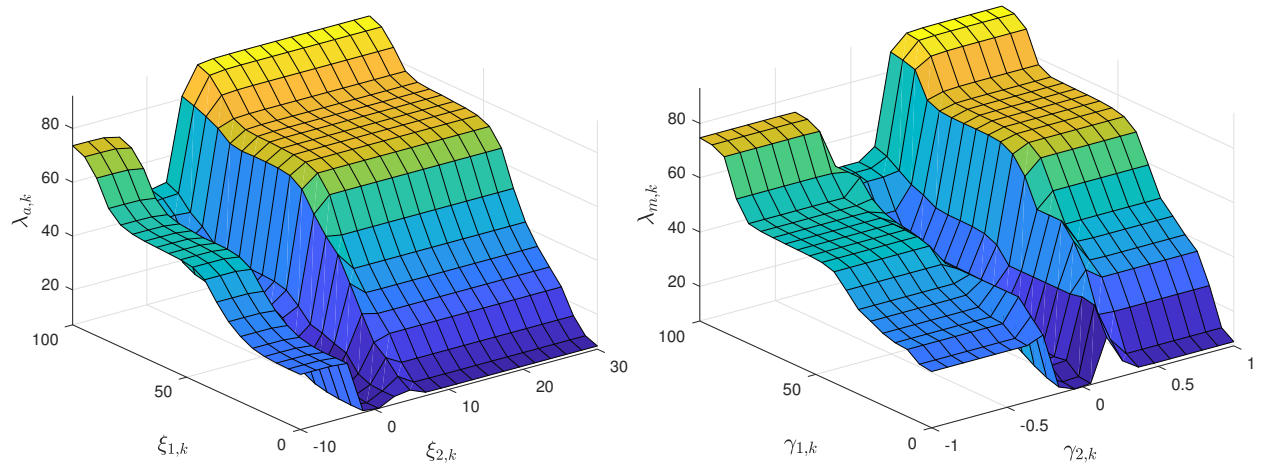
(a) (b) (c)

Fig. 2: (a) Fuzzy membership functions for input $\xi_{1,k}$, (b) Fuzzy membership functions for input $\xi_{2,k}$, and (c) Fuzzy membership functions for output $\lambda_{\mathbf{a},k}$.



(a) (b) (c)

Fig. 3: (a) Fuzzy membership functions for input $\gamma_{1,k}$, (b) Fuzzy membership functions for input $\gamma_{2,k}$, and (c) Fuzzy membership functions for output $\lambda_{\mathbf{m},k}$.



(a) (b)

Fig. 4: Surface map for (a) $\lambda_{\mathbf{a},k}$ and (b) $\lambda_{\mathbf{m},k}$.

acceleration and magnetic field from the accelerometer and magnetometer, respectively.

The fuzzy input parameters γ_1 and γ_2 are complementary. More specifically, γ_1 cannot be used to detect a disturbed magnetic field of the same magnitude but with a large dip angle deviation, and γ_2 cannot be used to detect a disturbed magnetic field with a small angle deviation but a large magnitude deviation. Thus, both parameters are required to detect magnetic field disturbances [38].

The fuzzy membership functions for the acceleration and magnetic field measurements have been designed based on experience and are shown in Tables I and II, respectively. The linguistic variable set of fuzzy inputs related to ξ_1 and γ_1 consists of the variables “Very Small (VS)”, “Small (S)”, “Medium (M)”, “Large (L)”, and “Very Large (VL)”, which represent the degree of angle deviation. The linguistic variable

1558-1748 (c) 2019 IEEE. Personal use is permitted, but republication/redistribution requires IEEE permission. See http://www.ieee.org/publications_standards/publications/rights/index.html for more information.

This article has been accepted for publication in a future issue of this journal, but has not been fully edited. Content may change prior to final publication. Citation information: DOI 10.1109/JSEN.2019.2947489, IEEE Sensors Journal

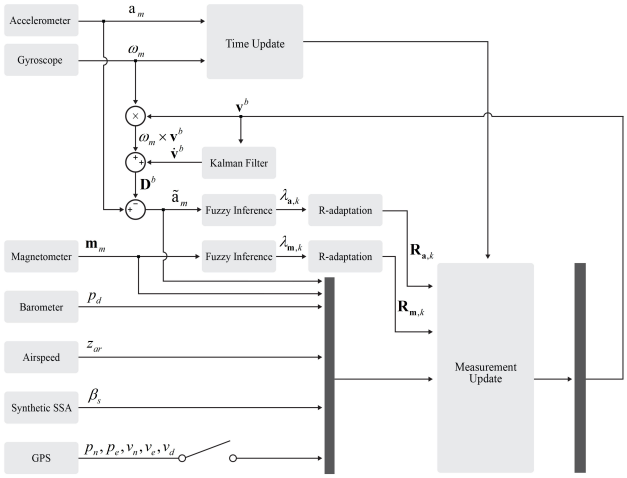


Fig. 5: Diagram of the proposed FAESKF algorithm.

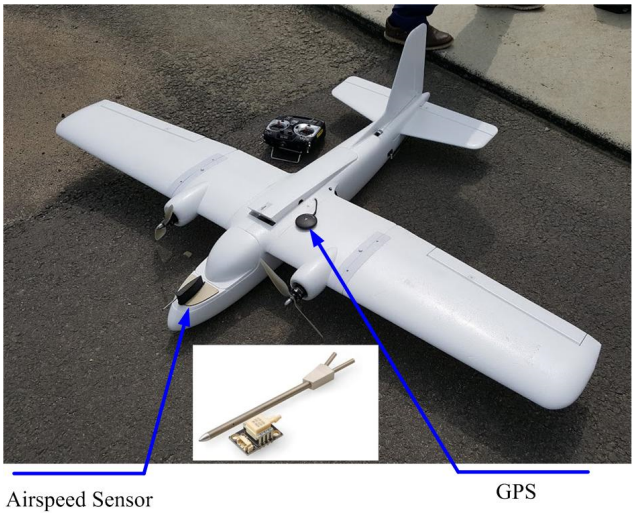


Fig. 6: Picture of the UAV platform and sensor system.

set related to ξ_2 and γ_2 consists of the variables "Minus", "Zero", and "Plus", which represent the direction of magnitude deviation. Generalized bell-shaped membership functions are utilized as the fuzzy membership functions for the inputs and the corresponding output $\lambda_{\mathbf{a},k}$, as shown in Fig. 2. The membership functions for the magnetic field are shown in Fig. 3. Fig. 4 depicts the surface maps for the acceleration and the magnetic field. The scaling factors $\lambda_{\mathbf{a},k}$ and $\lambda_{\mathbf{m},k}$, defined as the fuzzy outputs, are utilized to scale the measurement covariance matrix as follows:

$$\begin{aligned} \mathbf{R}_{\mathbf{a},k} &= \lambda_{\mathbf{a},k} \cdot \mathbf{R}_{\mathbf{a},0} \\ \mathbf{R}_{\mathbf{m},k} &= \lambda_{\mathbf{m},k} \cdot \mathbf{R}_{\mathbf{m},0} \end{aligned} \tag{36}$$

where $\mathbf{R}_{\mathbf{a},0} = \sigma_{\mathbf{a}}^2$ and $\mathbf{R}_{\mathbf{a},k}$ denote the nominal and resulting measurement covariances, respectively, for the acceleration and $\mathbf{R}_{\mathbf{m},0} = \sigma_{\mathbf{m}}^2$ and $\mathbf{R}_{\mathbf{m},k}$ similarly denote the nominal and resulting measurement covariances for the magnetic field.

By utilizing the proposed fuzzy inference rules, $\lambda_{\mathbf{a},k}$ and $\lambda_{\mathbf{m},k}$ are adaptively inferred depending on the fuzzy input parameters. More specifically, $\lambda_{\mathbf{a},k}$ adaptively increases when there is a significant gravity deviation, reducing the weight of the measured acceleration in the attitude estimation. Similarly, $\lambda_{\mathbf{m},k}$ adaptively increases when magnetic disturbance is detected, thus alleviating the undesirable effect of the disturbed magnetic field measurement on the attitude estimation.

TABLE III
UAV specifications

UAV parameter	Specification
Take-off weight	4.5 kg
Max. payload	2 kg
Wingspan	1800 mm
Flight time	90 minutes

TABLE IV
Detailed sensor data specifications

Sensor	Specifications
Barometer	Output rate: 10 Hz, $\sigma_b = 2\,\mathrm{m}$
Accelerometer	Output rate: 250 Hz, $\sigma_{\mathbf{a}} = 0.2\,\mathrm{m/s^2}$
Magnetometer	Output rate: 50 Hz, $\sigma_{\mathbf{m}} = 0.05$ gauss
Airspeed	Output rate: 10 Hz, $\sigma_{ar} = 1.4\,\mathrm{m/s}$
Synthetic SSA	Output rate: 10 Hz, $\sigma_s = 0.3\,\mathrm{rad}$

B. Fuzzy Adaptive Error-State Kalman Filter

A diagram of the overall architecture of the proposed FAESKF (Fuzzy Adaptive ESKF) algorithm is presented in Fig. 5. The acceleration and angular rate measurements are utilized for the time update. For the measurement update of the acceleration, $\mathbf{v}_k^b$ is computed using the FAESKF output state and the relationship in (27). Then, $\dot{\mathbf{v}}_k^b$ is estimated via the simple Kalman filter, treating $\mathbf{v}_k^b$ as an artificial measurement. Finally, the nongravitational acceleration vector $\mathbf{D}_k^b$ is subtracted from the raw acceleration to estimate the Earth's gravity.

The fuzzy input parameters are computed using the compensated acceleration $\tilde{\mathbf{a}}_m$ and the measured magnetic field $\mathbf{m}_m$ to detect gravitational and magnetic disturbances, respectively. Then, fuzzy outputs ($\lambda_{\mathbf{a},k}$ and $\lambda_{\mathbf{m},k}$) are computed based on the proposed fuzzy inference rules and are utilized to inflate the measurement noise to give less weight to disturbed measurements in the attitude estimation solution. The remaining measurements are the barometer, airspeed, and synthetic SSA measurements. The synthetic SSA measurement update is performed only when the predicted airspeed magnitude exceeds a certain threshold v_{th}, ensuring that the zero-angle assumption for the synthetic SSA is generally satisfied during straight and level flight. Note that the compensation of the bias states is omitted for simplicity in Fig. 5. The pseudocode of the proposed FAESKF algorithm is briefly summarized in Algorithm 1.

V. Experiments

Three sets of experimental flight tests were conducted using a custom-built fixed-wing UAV, as shown in Fig. 6. The UAV is equipped with a custom-built autopilot, an IMU (LSM303D

1558-1748 (c) 2019 IEEE. Personal use is permitted, but republication/redistribution requires IEEE permission. See http://www.ieee.org/publications_standards/publications/rights/index.html for more information.

This article has been accepted for publication in a future issue of this journal, but has not been fully edited. Content may change prior to final publication. Citation information: DOI 10.1109/JSEN.2019.2947489, IEEE Sensors Journal

integrated accelerometers/magnetometers and L3GD20 gyroscope), a barometer (MS5611, TE Connectivity), an airspeed sensor (MS4525DO, TE Connectivity), and a GPS receiver (NEO-M8N, u-blox). The general specifications of the fixed-wing UAV are summarized in Table III. The update rates of the IMU, magnetometer, barometer, airspeed sensor and GPS receiver are 250 Hz, 50 Hz, 10 Hz, 10 Hz, and 10 Hz, respectively. One-hour static experiment were conducted to perform the analysis of the Allan variance and the measurement and process noise characteristics of the sensors are summarized in Table IV and Table V, respectively. Note that the process noise of the wind states and scale factor are defined as: $\sigma_{\mathbf{v}_w} = 0.1\,\mathrm{m/s}^2$ and $\sigma_{w_s} = 0.1 \cdot 10^{-3}$.

Flight tests 1 and 2 were waypoint flights (autonomous flights) of relatively long and medium durations, respectively. Flight test 3 was a manual flight of short duration controlled by a pilot. Specifically, the flight times of the three experimental flight tests were 1,693 s, 653 s, and 326 s, respectively. The flight trajectories from these three experiments are shown in Fig. 7. Note that the flight trajectories from the three experimental flights do not involve any aggressive flight maneuvers, thus preventing excessive SSAs and ensuring the satisfaction of the assumption of a nearly zero SSA during flight. The attitude estimation from the GPS/INS Kalman filter [39] from the real flight was considered as the true attitude since the attitude estimation result of GPS/INS solution is not effected by nongravitational acceleration [23].

VI. Results and Discussion

To verify the superiority of the proposed FAESKF algorithm during a GPS outage, the conventional algorithm (Algorithm #1) [3] and the synthetic SSA algorithm (Algorithm #2) were implemented for a performance comparison. To demonstrate the effectiveness of the proposed algorithm, total GPS outages during flight were considered for all three flight tests; GPS measurements ($p_{n,k}$, $p_{e,k}$, $v_{n,k}$, $v_{e,k}$, and $v_{d,k}$) were intentionally not provided when running all filters with the recorded flight data.

In Algorithm #1, the raw acceleration measurements $\mathbf{a}_{m,k}$ are used to correct the roll and pitch angles. In Algorithm #2, the synthetic SSA measurements $\beta_{s,k}$ are additionally included. In the proposed FAESKF algorithm, both the compensated acceleration measurements $\tilde{\mathbf{a}}_{m,k}$ and the synthetic SSA measurements $\beta_{s,k}$ are utilized, and the fuzzy inference system is implemented. The measurements of all filters, including the ground truth, are summarized in Table VI.

All filters were implemented in MATLAB 2017b on a PC with an Intel Core i7-6500U CPU @2.50 GHz. The position error (PE), velocity error (VE), and root mean square errors (RMSEs) for the attitude were considered to evaluate the performance, as follows:

$$\begin{cases} \mathrm{PE}(k) = \sqrt{(p_{n,k} - \hat{p}_{n,k})^2 + (p_{e,k} - \hat{p}_{e,k})^2 + (p_{d,k} - \hat{p}_{d,k})^2} \\ \mathrm{VE}(k) = \sqrt{(v_{n,k} - \hat{v}_{n,k})^2 + (v_{e,k} - \hat{v}_{e,k})^2 + (v_{d,k} - \hat{v}_{d,k})^2} \\ \mathrm{RMSE} = \sqrt{\frac{1}{T}\sum_{k=1}^{T}(\mathbf{x}_k - \hat{\mathbf{x}}_k)^2} \end{cases}$$

Figs. 8(a), (b), and (c) depict the roll, pitch, and yaw angle estimation errors, respectively, during flight test 3. The attitude estimation results of Algorithm #2 are slightly better than those of Algorithm #1, and the proposed FAESKF algorithm shows a remarkable improvement in attitude estimation compared to the other algorithms. The RMSEs of the roll, pitch, and yaw angles in the three flight tests are summarized in Table VII. Overall, the proposed FAESKF algorithm yields the best attitude estimation results, and Algorithm #2 yields better attitude estimation results than Algorithm #1 algorithm does.

Figs. 9(a), (b), and (c) show the VEs during the three flight tests. The VEs of the proposed FAESKF algorithm again indicate the best estimation results, and Algorithm #2 presents better VE estimation results than Algorithm #1 does. Although position estimation is not the main focus of this paper, the proposed FAESKF algorithm also effectively mitigates the drift in the PE, whereas Algorithm #1 suffers from an unbounded increase in the PE during a GPS outage, as shown in Figs. 10(a), (b), and (c) for the three flight tests.

Figs. 11(a), (b), and (c) depict the innovation sequences and the corresponding $\pm 3\boldsymbol{\sigma}$ bounds of the innovation covariance for the synthetic SSA measurement update of the proposed algorithm during the three flight tests. The innovation sequence lies within the $\pm 3\boldsymbol{\sigma}$ bounds of the corresponding innovation covariance, demonstrating that the synthetic SSA measurement update of the proposed filter works consistently. Thus, it can be concluded that the synthetic SSA measurement as formulated under the zero-angle assumption is valid. Note that the synthetic SSA measurement update is performed only when the predicted airspeed magnitude is greater than a threshold of $v_{\mathrm{th}} = 7\ \mathrm{m/s}$. Also, note that the sudden increase of the innovation sequence occurs shortly when the synthetic SSA measurement update is initialized.

Figs. 12(a), (b), and (c) similarly depict the innovation sequences and the corresponding $\pm 3\boldsymbol{\sigma}$ bounds of the innovation covariance for the Kalman filter. Figs. 13(a), (b), and (c) show the estimation results for $v^b_{x,k}$, $v^b_{y,k}$, and $v^b_{z,k}$, respectively. The innovation sequence lies within the $\pm 3\boldsymbol{\sigma}$ bounds of the corresponding innovation covariance, proving that the proposed Kalman filter works consistently over the entire flight time. As shown, the longitudinal translation acceleration $v^b_{x,k}$ suddenly increases during climbing and descending and thus cannot be neglected, whereas $v^b_{y,k}$ is negligible compared to $v^b_{x,k}$ and $v^b_{z,k}$. These observations are consistent with the assumptions of previous studies [3], [40]. Thus, the uncompensated acceleration disturbed by nongravitational contributions may yield inaccurate roll and pitch angle estimates, particularly during climbing and descending.

Figs. 14(a) and (b) show the innovation sequence and the corresponding $\pm 3\boldsymbol{\sigma}$ bounds of the innovation covariance ($\mathbf{S}_k = \mathbf{H}_k\mathbf{P}_k^-\mathbf{H}_k^T + \mathbf{R}_k$) for the airspeed measurement update of the proposed algorithm during flight test 3 and the predicted and measured airspeeds, respectively. The innovation sequence lies within the $\pm 3\boldsymbol{\sigma}$ bounds of the corresponding innovation covariance, and the predicted airspeed closely matches the measured airspeed. The same phenomena were observed in the other flight tests; therefore, the corresponding data are omitted for simplicity. Thus, it can be concluded that the airspeed measurement formulation of the proposed filter, as given in

1558-1748 (c) 2019 IEEE. Personal use is permitted, but republication/redistribution requires IEEE permission. See http://www.ieee.org/publications_standards/publications/rights/index.html for more information.

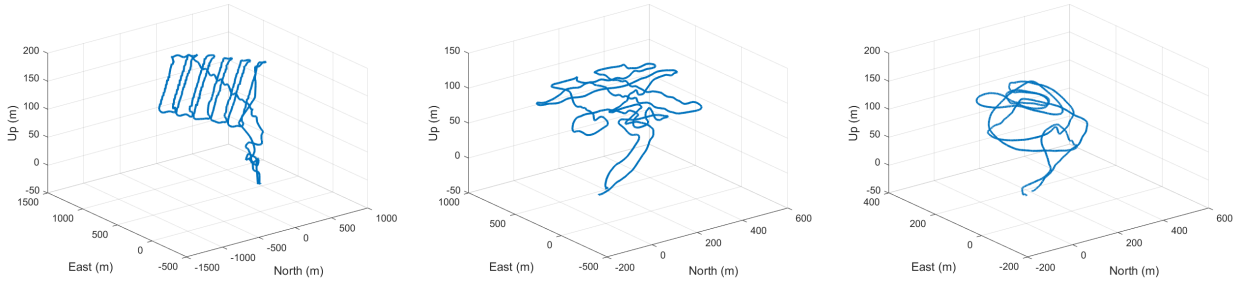
This article has been accepted for publication in a future issue of this journal, but has not been fully edited. Content may change prior to final publication. Citation information: DOI 10.1109/JSEN.2019.2947489, IEEE Sensors Journal

TABLE V
Detailed sensor data specification using Allan variance for the process noise

Accelerometer	Specification		
	X	Y	Z
Bias instability ($\sigma^2_{\mathbf{a}_n}$ [m/s^2])	$5.8732 \cdot 10^{-4}$	$4.6452 \cdot 10^{-4}$	$9.3451 \cdot 10^{-4}$
Velocity random work ($\sigma^2_{\mathbf{a}_\omega}$ [m/s$^2/\sqrt{\text{s}}$])	0.0016	0.0016	0.0028
Gyroscope	**Specification**		
	X	Y	Z
Bias instability ($\sigma^2_{\boldsymbol{\omega}_n}$ [rad/s])	$4.7324 \cdot 10^{-5}$	$4.7234 \cdot 10^{-5}$	$3.6552 \cdot 10^{-5}$
Angular random work ($\sigma^2_{\boldsymbol{\omega}_\omega}$ [rad/s$/\sqrt{\text{s}}$])	$1.1828 \cdot 10^{-4}$	$1.1694 \cdot 10^{-4}$	$1.1674 \cdot 10^{-4}$

TABLE VI
The measurement formulations for the different algorithms

	Algorithms	
	True	Algorithm #1
Measurement	$\mathbf{z}_{k,\text{normal}} = \begin{bmatrix} p_{n,k} \\ p_{e,k} \\ p_{d,k} \\ v_{n,k} \\ v_{d,k} \\ v_{e,k} \\ \mathbf{m}_{m,k} \\ z_{ar,k} \end{bmatrix}$ } GPS – Barometer } GPS – Magnetometer – Airspeed	$\mathbf{z}_{k,\text{GPS Outage}} = \begin{bmatrix} p_{d,k} \\ \mathbf{a}_{m,k} \\ \mathbf{m}_{m,k} \\ z_{ar,k} \end{bmatrix}$ – Barometer – Raw Accelerometer – Magnetometer – Airspeed
	Algorithms	
	Algorithm #2	Proposed
Measurement	$\mathbf{z}_{k,\text{GPS Outage}} = \begin{bmatrix} p_{d,k} \\ \mathbf{a}_{m,k} \\ \mathbf{m}_{m,k} \\ z_{ar,k} \\ \beta_{s,k} \end{bmatrix}$ – Barometer – Raw Accelerometer – Magnetometer – Airspeed – Synthetic SSA	$\mathbf{z}_{k,\text{GPS Outage}} = \begin{bmatrix} p_{d,k} \\ \tilde{\mathbf{a}}_{m,k} \\ \mathbf{m}_{m,k} \\ z_{ar,k} \\ \beta_{s,k} \end{bmatrix}$ – Barometer – Compensated Accelerometer – Magnetometer – Airspeed – Synthetic SSA



(a) (b) (c)

Fig. 7: Navigation trajectories for (a) flight test 1, (b) flight test 2, and (c) flight test 3.

TABLE VII
Comparison of attitude estimation performance

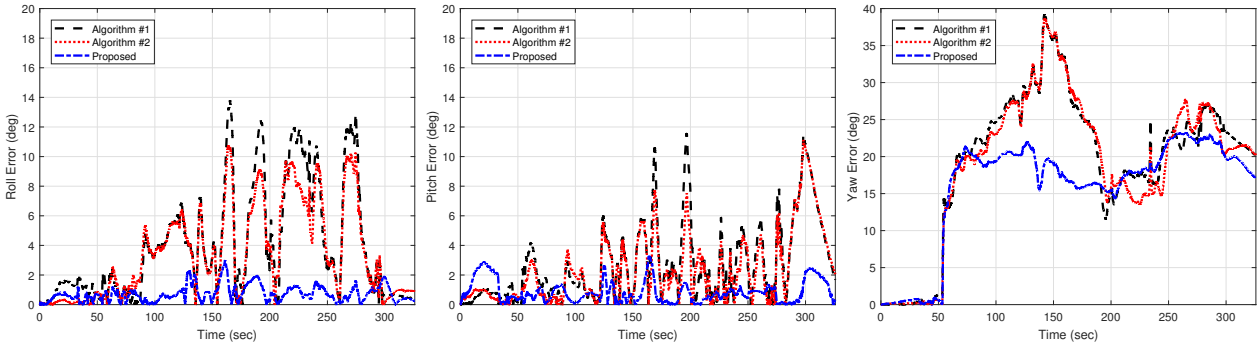
RMSE (°)	Flight Test 1			Flight Test 2			Flight Test 3		
	Algorithm #1	Algorithm #2	Proposed	Algorithm #1	Algorithm #2	Proposed	Algorithm #1	Algorithm #2	Proposed
Roll	1.7561	1.4654	0.6346	3.0425	2.4428	1.5431	5.4697	4.6594	0.9061
Pitch	2.2069	1.8447	0.9819	2.6863	2.5015	2.3008	3.7899	3.3568	1.1509
Yaw	15.7328	14.8102	13.3719	11.6694	11.2967	10.8350	21.8350	21.5967	17.5329

(30), works consistently.

Figs. 15(a), (b), and (c) show the calculated fuzzy inputs $\xi_{1,k}$ and $\xi_{2,k}$ and the fuzzy output $\lambda_{\mathbf{a},k}$, respectively, during flight test 3. It is seen that fuzzy output $\lambda_{\mathbf{a},k}$, which acts as a

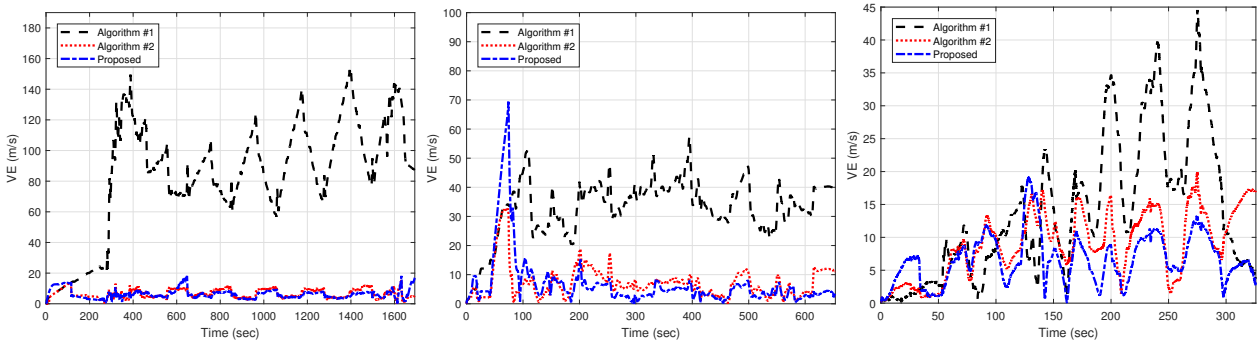
1558-1748 (c) 2019 IEEE. Personal use is permitted, but republication/redistribution requires IEEE permission. See http://www.ieee.org/publications_standards/publications/rights/index.html for more information.

This article has been accepted for publication in a future issue of this journal, but has not been fully edited. Content may change prior to final publication. Citation information: DOI 10.1109/JSEN.2019.2947489, IEEE Sensors Journal



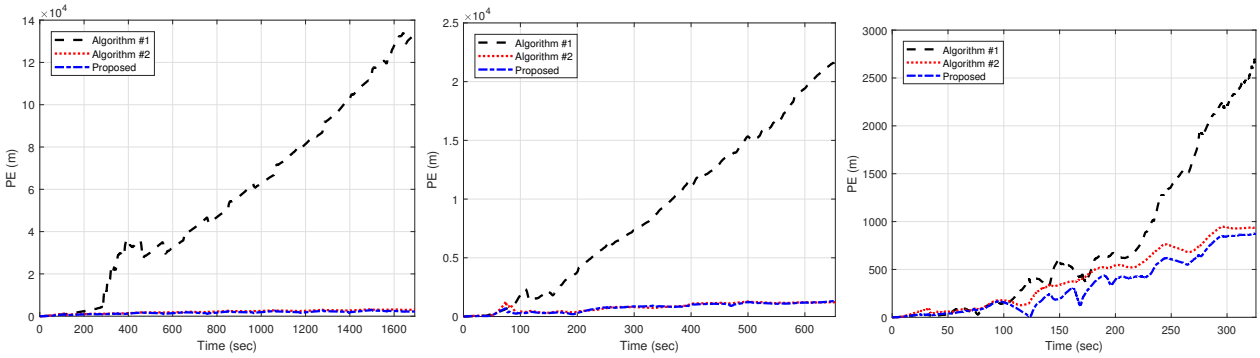
(a) (b) (c)

Fig. 8: Euler angle error estimation results during flight test 3 (a) roll, (b) pitch, and (c) yaw.



(a) (b) (c)

Fig. 9: VE estimation results for (a) flight test 1, (b) flight test 2, and (c) flight test 3.



(a) (b) (c)

Fig. 10: PE estimation results for (a) flight test 1, (b) flight test 2, and (c) flight test 3.

scaling factor, adaptively increases when significant deviations in magnitude and angle are identified based on the proposed fuzzy inference algorithm. Such an increase in the scaling factor $\lambda_{\mathbf{a},k}$ decreases the dependency of the attitude estimation on the disturbed acceleration measurement, thus improving the estimation performance.

Figs. 16(a) and (b) depict the calculated fuzzy inputs $\gamma_{1,k}$ and $\gamma_{2,k}$, respectively, during flight test 3. As shown, $\gamma_{1,k}$ and $\gamma_{2,k}$ are within the acceptable level range, meaning that no magnetic disturbance is evident since the magnetic interference from the power distribution board, motors, battery, and other electrical devices in the vicinity of the magnetometer of the UAV has been successfully minimized by twisting the wires and placing aluminum shielding around the wires. Therefore, the corresponding fuzzy inference for magnetic field disturbances was not actively applied in this experiment. In future work, artificial magnetic interference will be injected into the magnetic field measurements to verify the designed fuzzy logic for magnetic field disturbances.

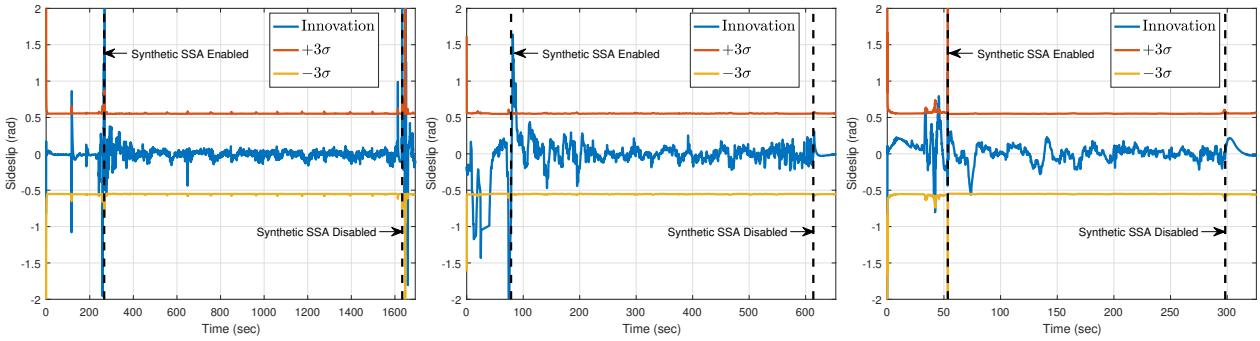
In particular, although the appropriate tuning of the fuzzy

TABLE VIII
Computation times per one cycle

	True (GPS/INS)	Algorithm #1	Algorithm #2	Proposed
Time (msec)	13.435	5.345	7.213	7.344

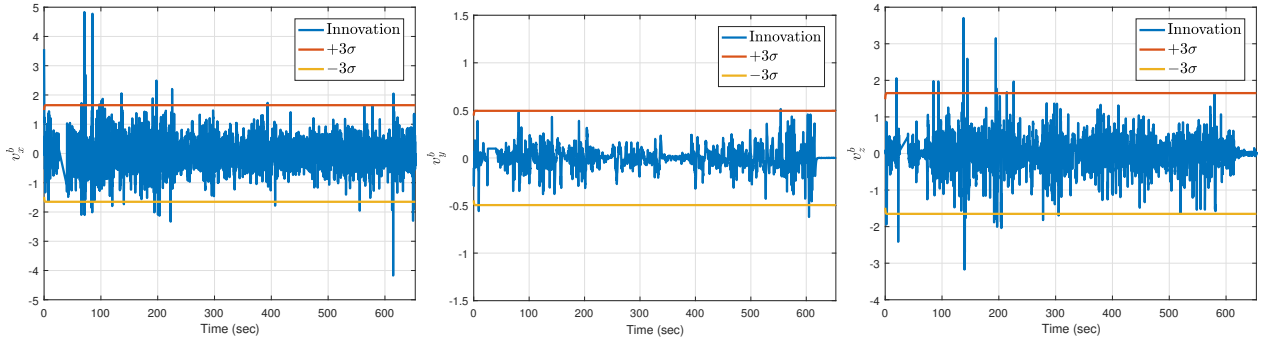
1558-1748 (c) 2019 IEEE. Personal use is permitted, but republication/redistribution requires IEEE permission. See http://www.ieee.org/publications_standards/publications/rights/index.html for more information.

This article has been accepted for publication in a future issue of this journal, but has not been fully edited. Content may change prior to final publication. Citation information: DOI 10.1109/JSEN.2019.2947489, IEEE Sensors Journal



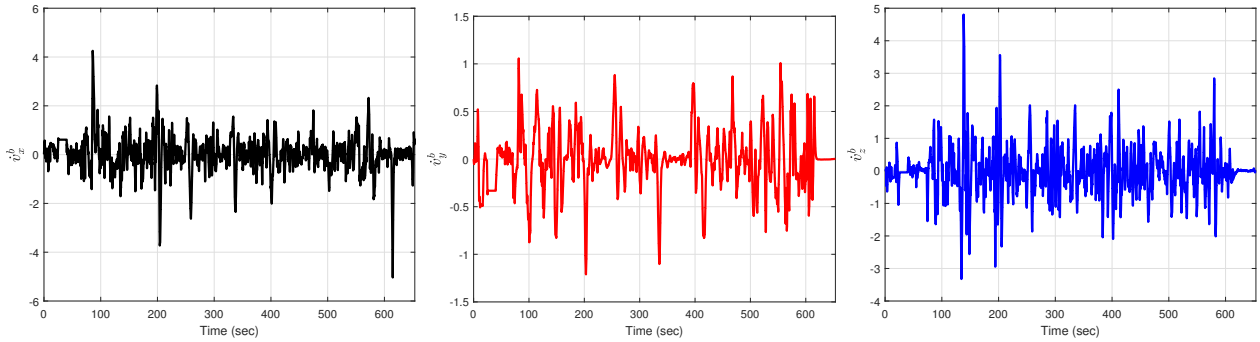
(a) (b) (c)

Fig. 11: Innovation sequences and corresponding $\pm 3\sigma$ bounds of the innovation covariance for (a) flight test 1, (b) flight test 2, and (c) flight test 3.



(a) (b) (c)

Fig. 12: Innovation sequences and corresponding $\pm 3\sigma$ bounds of the innovation covariance for (a) v_x^b, (b) v_y^b, and (c) v_z^b during flight test 2.



(a) (b) (c)

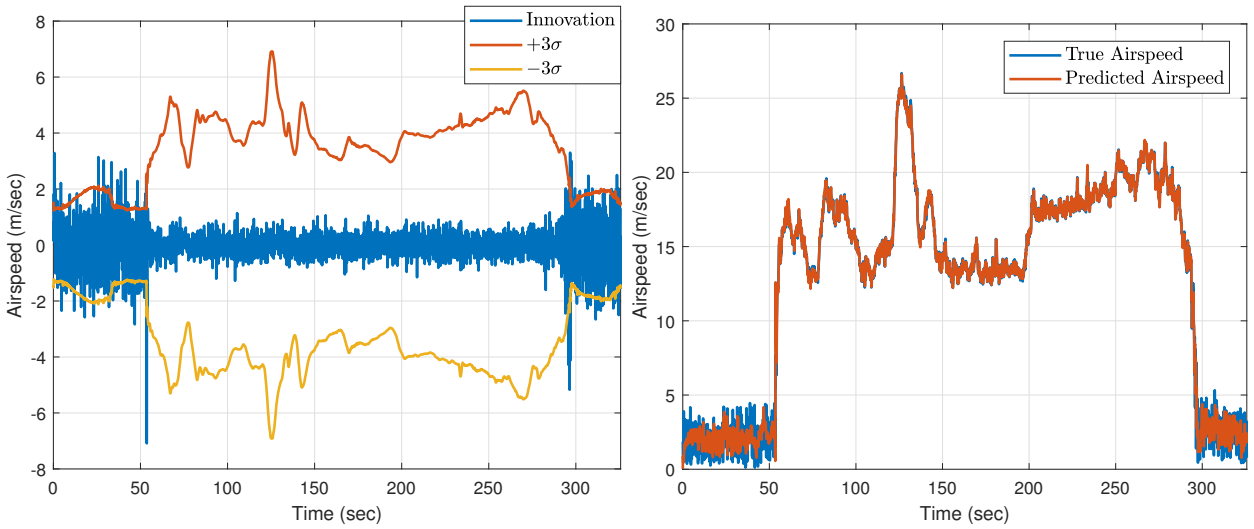
Fig. 13: Estimation results for (a) $\dot{v}_x^b$, (b) $\dot{v}_y^b$, and (c) $\dot{v}_z^b$ during flight test 2.

membership functions may result in the slight estimation performance improvement, the fuzzy membership functions of the proposed fuzzy inference algorithm do not need to be significantly re-designed for the different type of accelerometers and magnetometers due to the following reasons; regardless of the different type of accelerometers and magnetometers, the magnitude and direction of the compensated gravitational acceleration should closely match those of the true gravity vector and the magnitude and dip angle of the magnetic field should remain nearly constant with the assumption that the values of the Earth's magnetic field vector is constant. This assumption is valid since small UAV missions have been normally limited to restricted flying areas. In addition, the proposed fuzzy inference algorithm can be applied in other applications such as motion tracking since the above-mentioned principles are always valid.

Table VIII shows the computation times per one cycle of the IMU prediction for all algorithms. Considering that the GPS/INS Kalman filter (24-states) runs in real time on a custom-built autopilot (168 MHz, 32bit STM32F427 ARM Cortex-M4F core with FPU (Floating Point Unit)) during the real flight test, it can be deduced that the proposed algorithm also can be implemented on the autopilot in real time.

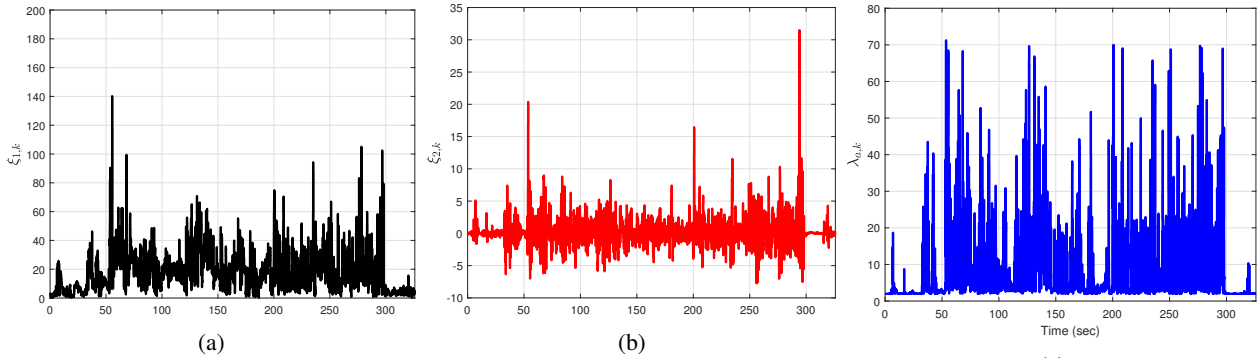
1558-1748 (c) 2019 IEEE. Personal use is permitted, but republication/redistribution requires IEEE permission. See http://www.ieee.org/publications_standards/publications/rights/index.html for more information.

This article has been accepted for publication in a future issue of this journal, but has not been fully edited. Content may change prior to final publication. Citation information: DOI 10.1109/JSEN.2019.2947489, IEEE Sensors Journal



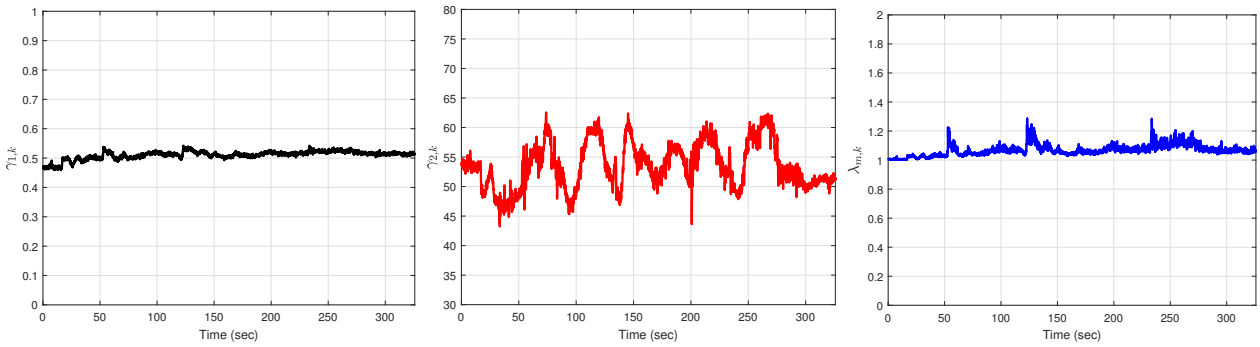
(a) (b)

Fig. 14: (a) Innovation analysis for flight test 3. (b) Predicted and measured airspeeds during flight test 3.



(a) (b) (c)

Fig. 15: (a) Fuzzy input ξ_1, (b) fuzzy input ξ_2, and (c) fuzzy output $\lambda_{\mathbf{a},k}$ during flight test 3.



(a) (b) (c)

Fig. 16: (a) Fuzzy input γ_1, (b) fuzzy input γ_2, and (c) fuzzy output $\lambda_{\mathbf{m},k}$ during flight test 3.

VII. Conclusion

This paper presents a fuzzy adaptive attitude estimation algorithm for use during a GPS outage. Specifically, a synthetic SSA measurement formulation is first proposed to improve the estimation performance during a GPS outage. This formulation is based on the assumption that the flight trajectories of small UAVs do not involve extreme aggressive maneuvers, such as abrupt changes in the aircraft's attitude, abnormal attitudes, or abnormal acceleration, meaning that the SSA is negligible. It is observed that the proposed synthetic SSA measurement formulation enables significant improvements in velocity/position estimation as well as attitude estimation compared with the conventional algorithms. In addition, the validity of the synthetic SSA measurement approach is analyzed based on a filter consistency analysis using data from three flight tests. To achieve the required performance, the

1558-1748 (c) 2019 IEEE. Personal use is permitted, but republication/redistribution requires IEEE permission. See http://www.ieee.org/publications_standards/publications/rights/index.html for more information.

This article has been accepted for publication in a future issue of this journal, but has not been fully edited. Content may change prior to final publication. Citation information: DOI 10.1109/JSEN.2019.2947489, IEEE Sensors Journal

proper installation and calibration of AOA/SSA sensors require extensive effort and incur a high cost; consequently, the use of such sensors is impractical for small, low-cost UAVs. As an alternative, the proposed synthetic SSA measurement approach can be regarded as equivalent to a virtual SSA sensor that can enhance the estimation performance for a small, low-cost UAV without actual AOA/SSA sensors during a GPS outage.

In addition, the nongravitational acceleration component, defined as a disturbance, is estimated using a simple Kalman filter and is then used to correct the raw accelerometer measurement to obtain a reliable estimate of the Earth's gravity. Then, a fuzzy adaptive inference algorithm is implemented to detect disturbances in the acceleration and magnetic field measurements and to inflate the measurement covariance accordingly with the assumption that the values of the Earth's magnetic field vector are constant. The proposed FAESKF algorithm achieves remarkable improvements in attitude and velocity estimation during a GPS outage compared to the conventional algorithms. In addition, the drift in the estimated position is effectively mitigated by the proposed algorithm. However, the zero-angle assumption for the synthetic SSA approach may no longer be satisfied during aggressive flights, which will cause both the attitude error and the velocity/position errors to increase. In the future, the proposed FAESKF algorithm will be applied to data recorded during extreme aggressive flight maneuvers to further evaluate its validity.

REFERENCES

[1] M. Barczyk and A. F. Lynch, "Integration of a triaxial magnetometer into a helicopter UAV GPS-aided INS," *IEEE Trans. Aerosp. Electron. Syst.*, vol. 48, no. 4, pp. 2947–2960, Oct. 2012.

[2] J. Wu, Z. Zhou, B. Gao, R. Li, Y. Cheng, and H. Fourati, "Fast linear quaternion attitude estimator using vector observations," *IEEE Trans. Autom. Sci. Eng.*, vol. 15, no. 1, pp. 307–319, Jan. 2018.

[3] H. G. De Marina, F. J. Pereda, J. M. Giron-Sierra, and F. Espinosa, "UAV attitude estimation using unscented Kalman filter and TRIAD," *IEEE Trans. Ind. Electron.*, vol. 59, no. 11, pp. 4465–4474, Nov. 2012.

[4] K. H. Kim, J. G. Lee, and C. G. Park, "Adaptive two-stage extended Kalman filter for a fault-tolerant INS-GPS loosely coupled system," *IEEE Trans. Aerosp. Electron. Syst.*, vol. 45, no. 1, pp. 125–137, Jan. 2009.

[5] J. S. Jang and D. Liccardo, "Small UAV automation using MEMS," *IEEE Aerosp. Electron. Syst. Mag.*, vol. 22, no. 5, pp. 30–34, Jun. 2007.

[6] Z. Wu, M. Yao, H. Ma, W. Jia, and F. Tian, "Low-cost antenna attitude estimation by fusing inertial sensing and two-antenna GPS for vehicle-mounted satcom-on-the-move," *IEEE Trans. Veh. Technol.*, vol. 62, no. 3, pp. 1084–1096, Mar. 2013.

[7] R. Mahony, M. Euston, J. Kim, P. Coote, and T. Hamel, "A non-linear observer for attitude estimation of a fixed-wing unmanned aerial vehicle without GPS measurements," *Trans. Inst. Meas. Control*, vol. 33, no. 6, pp. 699–717, Aug. 2011.

[8] Y.-C. Lai and S.-S. Jan, "Attitude estimation based on fusion of gyroscopes and single antenna GPS for small UAVs under the influence of vibration," *GPS Solut.*, vol. 15, no. 1, pp. 67–77, Jan. 2011.

[9] P. Marantos, Y. Koveos, and K. J. Kyriakopoulos, "UAV state estimation using adaptive complementary filters," *IEEE Trans. Control Syst. Technol.*, vol. 24, no. 4, pp. 1214–1226, Jul. 2016.

[10] J. Wu, Z. Zhou, J. Chen, H. Fourati, and R. Li, "Fast complementary filter for attitude estimation using low-cost MARG sensors," *IEEE Sensors J.*, vol. 16, no. 18, pp. 6997–7007, Sept. 2016.

[11] Y. S. Suh, "Orientation estimation using a quaternion-based indirect Kalman filter with adaptive estimation of external acceleration," *IEEE Trans. Instrum. Meas.*, vol. 59, no. 12, pp. 3296–3305, Dec. 2010.

[12] H. Zhao and Z. Wang, "Motion measurement using inertial sensors, ultrasonic sensors, and magnetometers with extended Kalman filter for data fusion," *IEEE Sensors J.*, vol. 12, no. 5, pp. 943–953, May 2012.

[13] W. Zhao, Z. Fang, and P. Li, "Bridging GPS outages for fixed-wing unmanned aerial vehicles," *J. Navig.*, vol. 68, no. 2, pp. 308–326, Mar. 2015.

[14] S. Lee and S. Hong, "Velocity-aided attitude estimation for helicopter aircraft using microelectromechanical system inertial-measurement units," *Sensors*, vol. 16, no. 12, p. 2102, Dec. 2016.

[15] L. Chen and J. Fang, "A hybrid prediction method for bridging GPS outages in high-precision POS application," *IEEE Trans. Instrum. Meas.*, vol. 63, no. 6, pp. 1656–1665, Jun. 2014.

[16] W. Ye, Z. Liu, C. Li, and J. Fang, "Enhanced Kalman filter using noisy input gaussian process regression for bridging GPS outages in a POS," *J. Navig.*, vol. 71, no. 3, pp. 565–584, May 2018.

[17] Q. Xu, X. Li, and C.-Y. Chan, "Enhancing localization accuracy of MEMS-INS/GPS/in-vehicle sensors integration during GPS outages," *IEEE Trans. Instrum. Meas.*, vol. 67, no. 8, pp. 1966–1978, Aug. 2018.

[18] G. Araguás, C. Paz, D. Gaydou, and G. P. Paina, "Quaternion-based orientation estimation fusing a camera and inertial sensors for a hovering UAV," *J. Intell. Robotic Syst.*, vol. 77, no. 1, pp. 37–53, Jan. 2015.

[19] V. Madyastha, V. Ravindra, S. Mallikarjunan, and A. Goyal, "Extended Kalman filter vs. error state Kalman filter for aircraft attitude estimation," in *Proc. AIAA Guidance, Navigation, and Control Conference*, Portland, Oregon, p. 6615, 2011.

[20] N. Trawny and S. I. Roumeliotis, "Indirect Kalman filter for 3D attitude estimation," University of Minnesota, Dept. of Comp. Sci. & Eng., Tech. Rep, vol. 2, 2005.

[21] A. Santamaria-Navarro, G. Loianno, J. Solà, V. Kumar, and J. Andrade-Cetto, "Autonomous navigation of micro aerial vehicles using high-rate and low-cost sensors," *Auton. Robots*, vol. 42, no. 6, pp. 1263–1280, Aug. 2018.

[22] F. L. Markley, "Attitude error representations for Kalman filtering," *J. Guid. Control Dyn.*, vol. 26, no. 2, pp. 311–317, 2003.

[23] H. No, A. Cho, and C. Kee, "Attitude estimation method for small UAV under accelerative environment," *GPS Solut.*, vol. 19, no. 3, pp. 343–355, Jul. 2015.

[24] W. Li and J. Wang, "Effective adaptive Kalman filter for MEMS-IMU/magnetometers integrated attitude and heading reference systems," *J. Navig.*, vol. 66, no. 1, pp. 99–113, Jan. 2013.

[25] A. Cho, J. Kim, S. Lee, and C. Kee, "Wind estimation and airspeed calibration using a UAV with a single-antenna GPS receiver and pitot tube," *IEEE Trans. Aerosp. Electron. Syst.*, vol. 47, no. 1, pp. 109–117, Jan. 2011.

[26] S. Weiss, M. W. Achtelik, S. Lynen, M. C. Achtelik, L. Kneip, M. Chli, and R. Siegwart, "Monocular vision for long-term micro aerial vehicle state estimation: A compendium," *J. Field Robot.*, vol. 30, no. 5, pp. 803–831, Oct. 2013.

[27] G. Zhang and L.-T. Hsu, "Intelligent GNSS/INS integrated navigation system for a commercial UAV flight control system," *Aerosp. Sci. Technol.*, vol. 80, pp. 368–380, Sept. 2018.

[28] J. L. Crassidis and J. L. Junkins, *Optimal Estimation of Dynamic Systems*. Boca Raton, FL: Chapman and Hall/CRC, 2004.

[29] M. B. Rhudy, Y. Gu, J. N. Gross, and H. Chao, "Onboard wind velocity estimation comparison for unmanned aircraft systems," *IEEE Trans. Aerosp. Electron. Syst.*, vol. 53, no. 1, pp. 55–66, Feb. 2017.

[30] M. Euston, P. Coote, R. Mahony, J. Kim, and T. Hamel, "A complementary filter for attitude estimation of a fixed-wing UAV," in *2008 IEEE/RSJ International Conference on Intelligent Robots and Systems*, pp. 340–345. Nice, France: IEEE, 2008.

[31] A. M. Sabatini, "Quaternion-based extended Kalman filter for determining orientation by inertial and magnetic sensing," *IEEE Trans. Biomed. Eng.*, vol. 53, no. 7, pp. 1346–1356, Jul. 2006.

[32] A. Makni, H. Fourati, and A. Y. Kibangou, "Energy-aware adaptive attitude estimation under external acceleration for pedestrian navigation," *IEEE/ASME Trans. Mechatronics*, vol. 21, no. 3, pp. 1366–1375, Jun. 2016.

[33] P. Appel, "Attitude estimation from magnetometer and earth-albedo-corrected coarse sun sensor measurements," *Acta Astronaut.*, vol. 56, no. 1-2, pp. 115–126, Jan. 2005.

[34] D. Gebre-Egziabher and G. H. Elkaim, "MAV attitude determination by vector matching," *IEEE Trans. Aerosp. Electron. Syst.*, vol. 44, no. 3, pp. 1012–1028, Jul. 2008.

[35] E. H. Mamdani and S. Assilian, "An experiment in linguistic synthesis with a fuzzy logic controller," *Int. J. Man-Mach. Stud.*, vol. 7, no. 1, pp. 1–13, Jan. 1975.

[36] L. A. Zadeh, "Outline of a new approach to the analysis of complex systems and decision processes," *IEEE Trans. Syst. Man Cybern.*, no. 1, pp. 28–44, Jan. 1973.

1558-1748 (c) 2019 IEEE. Personal use is permitted, but republication/redistribution requires IEEE permission. See http://www.ieee.org/publications_standards/publications/rights/index.html for more information.

This article has been accepted for publication in a future issue of this journal, but has not been fully edited. Content may change prior to final publication. Citation information: DOI 10.1109/JSEN.2019.2947489, IEEE Sensors Journal

[37] N. Yadav and C. Bleakley, "Accurate orientation estimation using AHRS under conditions of magnetic distortion," *Sensors*, vol. 14, no. 11, pp. 20008–20024, Jan. 2014.
[38] B. Fan, Q. Li, C. Wang, and T. Liu, "An adaptive orientation estimation method for magnetic and inertial sensors in the presence of magnetic disturbances," *Sensors*, vol. 17, no. 5, p. 1161, May 2017.
[39] S. Weiss, M. W. Achtelik, S. Lynen, M. C. Achtelik, L. Kneip, M. Chli, and R. Siegwart, "Monocular vision for long-term micro aerial vehicle state estimation: A compendium," *J. Field Robot.*, vol. 30, no. 5, pp. 803–831, Aug. 2013.
[40] H. Sheng and T. Zhang, "MEMS-based low-cost strap-down AHRS research," *Measurement*, vol. 59, pp. 63–72, Jan. 2015.



Wonkeun Youn received his B.S. degree from Handong Global University, Pohang, South Korea, in 2008 and his M.S. degree from the Korea Advanced Institute of Science and Technology (KAIST), Daejeon, South Korea, in 2010.

He has been a Senior Researcher with the UAV System Division, Korea Aerospace Research Institute (KARI), since 2011 and is currently pursuing his Ph.D. degree in the Department of Robotics Program at KAIST. His current research interests include multisensor fusion, Bayesian estimation theory, multimodal target tracking, and GPS/INS-based UAV navigation.



Matthew B. Rhudy received the B.S. degree in mechanical engineering from Pennsylvania State University, State College, PA, USA, the M.S. degree in mechanical engineering from the University of Pittsburgh, Pittsburgh, PA, USA, and the Ph.D. degree in aerospace engineering from West Virginia University, Morgantown, WV, USA, in 2008, 2009, and 2013, respectively. From 2013 to 2015, he worked as a Visiting Assistant Professor in the Department of Mechanical Engineering, Lafayette College, Easton, PA, USA. Since 2015, he has been an Assistant Professor in the Division of Engineering, Pennsylvania State University, Reading, PA, USA.



Am Cho received his received B.S., M.S., and Ph.D. degrees from Seoul National University (SNU) in 2010, Seoul, South Korea. He was a leader of the UAV team in the GNSS Laboratory. He has been a Senior Researcher with the UAV System Division, Korea Aerospace Research Institute (KARI) since 2010. His research interests include GPS/INS integration and automatic flight control systems for UAVs.



HYUN MYUNG received the B.S., M.S., and Ph.D. degrees in electrical engineering from the Korea Advanced Institute of Science and Technology (KAIST), Daejeon, Korea, in 1992, 1994, and 1998, respectively. He was a Senior Researcher with the Electronics and Telecommunications Research Institute, Daejeon, from 1998 to 2002, a CTO and the Director with the Digital Contents Research Laboratory, Emersys Corporation, Daejeon, from 2002 to 2003, and a Principle Researcher with the Samsung Advanced Institute of Technology, Yongin, Korea, from 2003 to 2008. Since 2008, he has been a Professor with the Department of Civil and Environmental Engineering, KAIST, and he is the Head of the KAIST Robotics Program. From 2019, he is a Professor with the School of Electrical Engineering. His current research interests include autonomous robot navigation, SLAM (simultaneous localization and mapping), SHM (structural health monitoring), machine learning, AI, and swarm robots.

1558-1748 (c) 2019 IEEE. Personal use is permitted, but republication/redistribution requires IEEE permission. See http://www.ieee.org/publications_standards/publications/rights/index.html for more information.